

LRP 493/94

July 1994

Invited and Contributed Papers  
presented at the  
21st EPS CONFERENCE ON CONTROLLED  
FUSION AND PLASMA PHYSICS

Montpellier, France  
27 June - 1 July, 1994

## LIST OF CONTENTS

	<u>Page</u>
- CREATION AND CONTROL OF VARIABLY SHAPED PLASMAS IN TCV Invited Paper by <i>F. Hofmann, J.B. Lister, M. Anton, S. Barry, R. Behn, S. Bernel, G. Besson, F. Bühlmann, R. Chavan, M. Corboz, M.J. Dutch, B.P. Duval, D. Fasel, A. Favre, S. Franke, A. Heym, A. Hirt, Ch. Hollenstein, P. Isoz, B. Joye, X. Llobet, J.C. Magnin, B. Marletaz, Ph. Marmillod, Y. Martin, J.M. Mayor, J.M. Moret, Ch. Nieswand, P.J. Paris, A. Perez, Z.A. Pietrzyk, R.A. Pitts, A. Pochelon, R. Rage, O. Sauter, G. Tonetti, M.Q. Tran, F. Troyon, D.J. Ward, H. Weisen</i>	01
- THE THOMSON SCATTERING DIAGNOSTIC ON THE TCV TOKAMAK <i>R. Behn, S. Franke, Z.A. Pietrzyk</i>	13
- EXPERIMENTAL STUDY OF ION PHASE SPACE IN THE APPROACH TO LARGE SCALE CHAOS IN WAVE-PARTICLE INTERACTION <i>A.F. Fasoli, F.N. Skiff</i>	17
- MEASUREMENT OF THE OPTICAL DEPTH AT THE THIRD ELECTRON CYCLOTRON HARMONIC IN TORE SUPRA <i>J.L. Ségui, Y. Michelot, G. Giruzzi, T. Goodman, A. Kritz, A. Pochelon, O. Sauter, G.R. Smith, M.Q. Tran</i>	21
- THE DYNAMICS OF SHAPING CONTROL IN TCV <i>J.B. Lister, Y. Martin, J.-M. Moret</i>	25
- STUDIES OF THE DENSITY LIMIT OF ELONGATED PLASMAS IN TCV USING A FIR INTERFEROMETER <i>C. Nieswand, R. Behn, F. Buhlmann, F. Hofmann, Y. Martin</i>	29

- IDEAL MHD STABILITY IN TOKAMAKS WITH EXTERNAL HELICAL WINDINGS 33  
*R. Moeckli, W.A. Cooper, F. Troyon*
- MHD LIMITS AND AXISYMMETRIC STABILITY OF DOUBLETS 37  
*L. Degtyarev, A. Martynov, S. Medvedev, F. Troyon, L. Villard*
- STABILIZATION OF PRESSURE-DRIVEN EXTERNAL MODES IN TOKAMAKS WITH A RESISTIVE WALL AND TOROIDAL ROTATION 41  
*D.J. Ward, A. Bondeson*
- TEARING STABILITY OF AN ITER SHAPED PLASMA 45  
*A. Pletzer, J. Manickam, D.A. Monticello*

## Creation and Control of Variably Shaped Plasmas in TCV

F. Hofmann, J.B. Lister, M. Anton, S. Barry, R. Behn, S. Bernel, G. Besson, F. Bühlmann, R. Chavan, M. Corboz, M.J. Dutch, B.P. Duval, D. Fasel, A. Favre, S. Franke, A. Heym, A. Hirt, Ch. Hollenstein, P. Isoz, B. Joye, X. Llobet, J.C. Magnin, B. Marletaz, Ph. Marmillod, Y. Martin, J.M. Mayor, J.M. Moret, Ch. Nieswand, P.J. Paris, A. Perez, Z.A. Pietrzyk, R.A. Pitts, A. Pochelon, R. Rage, O. Sauter, G. Tonetti, M.Q. Tran, F. Troyon, D.J. Ward, H. Weisen

Centre de Recherches en Physique des Plasmas  
Ecole Polytechnique Fédérale de Lausanne  
Association EURATOM-Confédération Suisse  
21 Avenue des Bains, CH-1007 Lausanne, Switzerland

**Abstract:** During the first year of operation, the TCV tokamak has produced a large variety of plasma shapes and magnetic configurations, with  $1.0 \leq B \leq 1.46\text{T}$ ,  $I \leq 800\text{kA}$ ,  $\kappa \leq 2.05$ ,  $-0.7 \leq \delta \leq 0.7$ . A new shape control algorithm, based on a finite element reconstruction of the plasma current in real time, has been implemented. Vertical growth rates of  $800 \text{ sec}^{-1}$ , corresponding to a stability margin  $f=1.15$ , have been stabilized. Ohmic H-modes, with energy confinement times reaching 80ms, normalized beta ( $\beta_{aB/I_p}$ ) of 1.9 and  $\tau_E/ITER89\text{-P}$  of 2.4 have been obtained in single-null X-point deuterium discharges with the ion grad B drift towards the X-point. Limiter H-modes with maximum line averaged electron densities of  $1.7 \times 10^{20} \text{ m}^{-3}$  have been observed in D-shaped plasmas with  $360\text{kA} \leq I_p \leq 600\text{kA}$ .

### 1. Introduction

TCV is a compact, highly elongated tokamak, capable of producing limited or diverted plasmas with currents up to 1 MA. Since the main aim of TCV is to investigate effects of plasma shape on tokamak physics, the machine has been designed such that it can produce diverse plasma shapes without requiring hardware modifications. This versatility can easily be achieved for plasmas with moderate elongation, but for highly elongated plasmas, a close fitting passive shell becomes necessary, which is clearly in conflict with the idea of variable shape. The design of TCV can be considered as a compromise between maximum shape variability and a good passive vertical stability.

In order to satisfy these conflicting requirements, TCV incorporates a number of unusual design features: The poloidal field system consists of an OH transformer and sixteen independently driven shaping coils located between the vacuum vessel and the toroidal field coils. The vacuum vessel is a continuously welded structure with low toroidal resistance ( $55 \mu \text{ Ohms}$ ) and a nearly rectangular cross-section (height to width ratio of 3). First wall protection consists of high purity, isotropic graphite tiles

covering the vessel inboard wall and floor, together with a full toroidal belt limiter mounted on the outboard wall 23 cm below the midplane. In addition, eight symmetrically disposed, full poloidal bands of tiles afford some protection at the top of the vessel and cover the in-vessel poloidal magnetic field probe arrays. Two fast acting coils will be installed later this year inside the vessel to stabilize rapidly growing vertical modes. Installation of an ECRH system (4.5 MW) will begin in 1995.

TCV produced its first plasma in November 1992, with full tokamak operation starting in June 1993. During the first experimental campaign (June 1993 - November 1993), plasma breakdown and current ramp-up conditions were optimized and D-shaped plasmas with  $I_p \leq 700\text{kA}$ ,  $\kappa \leq 2.0$  were produced. Most of these plasmas were limited on the inner wall of the vacuum vessel. TCV operation was suspended between November 1993 and February 1994 for the installation of additional diagnostics (Thomson scattering [1], FIR interferometer [2], camera ports, etc.). The second experimental campaign was mainly devoted to the optimization of the vertical position control system and to the creation of single-null divertor configurations, suitable for ohmic H-mode operation. The TCV vacuum vessel was boronized for the first time in May 1994 by means of a standard glow discharge in a 10%  $B_2H_6$  / 90% He gas mixture.

In this paper, section 2 briefly describes the methods used to create highly elongated and shaped plasmas, and section 3 discusses the vertical stability and the limits of plasma current and elongation imposed by our present system. In section 4, the results on the ohmic H-mode in TCV are presented and in section 5, we give a preliminary analysis of energy confinement time in various types of discharges.

## 2. Shape Control

There are probably as many methods for plasma shape control as there are shaped tokamaks in the world [3-9] but they can be broadly divided into two categories. In the first are algorithms which use a large database of precalculated equilibria to obtain shape parameters from the measurements. This can be achieved in several different ways, using, for example, Singular Value Decomposition [5], Function Parametrization [8], Neural Networks [6,7], etc. In the second category are methods which determine the plasma shape without reference to a database, such as a local expansion of the flux function [3] or an approximate reconstruction of the plasma current in real time [9].

In TCV many of these methods can be tested. Here, we shall only discuss one particular algorithm [9], i.e. the one used almost exclusively by the experiments described in this paper. This algorithm is based on a finite element reconstruction of the plasma current [10], performed in real time by an analog-digital hybrid computer. The reconstructed plasma current distribution can then be used either to compute global shape parameters (e.g. radial position, vertical position, elongation, triangularity, etc.) or to calculate flux errors at the plasma boundary. In the former case, the coil currents must be essentially preprogrammed, and corrections are applied in the form of moments (radial field, vertical field, quadrupole field, etc.). The strength of these moments depends on the difference between the actual shape parameters and their preprogrammed values. In the latter case, the coil current corrections are computed such as to minimize the flux errors at the plasma boundary. This second algorithm, however, is highly non-linear since the plasma shape changes with time and the points at which the flux errors must be evaluated move together with the plasma boundary.

To date, the moments method has been found to be sufficient for the relatively uncomplicated plasma shapes explored. Figure 1 shows pre-programmed and

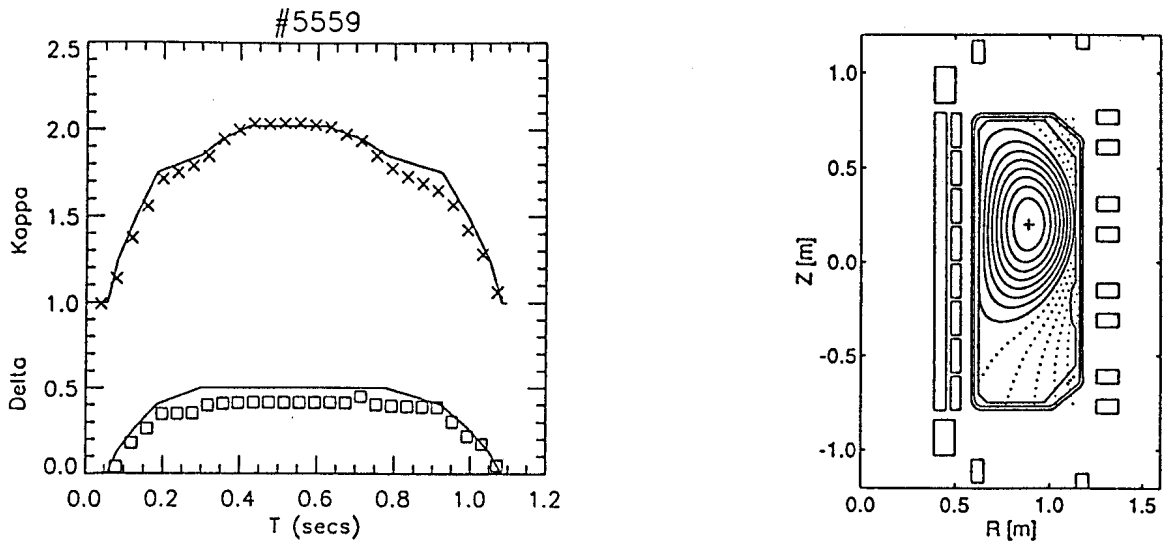


Figure 1. (a) Preprogrammed (lines) and measured (symbols) shape parameters for limiter discharge with  $I_p(\text{max})=810\text{kA}$  (b) Magnetic configuration at  $t=0.5\text{sec}$ .

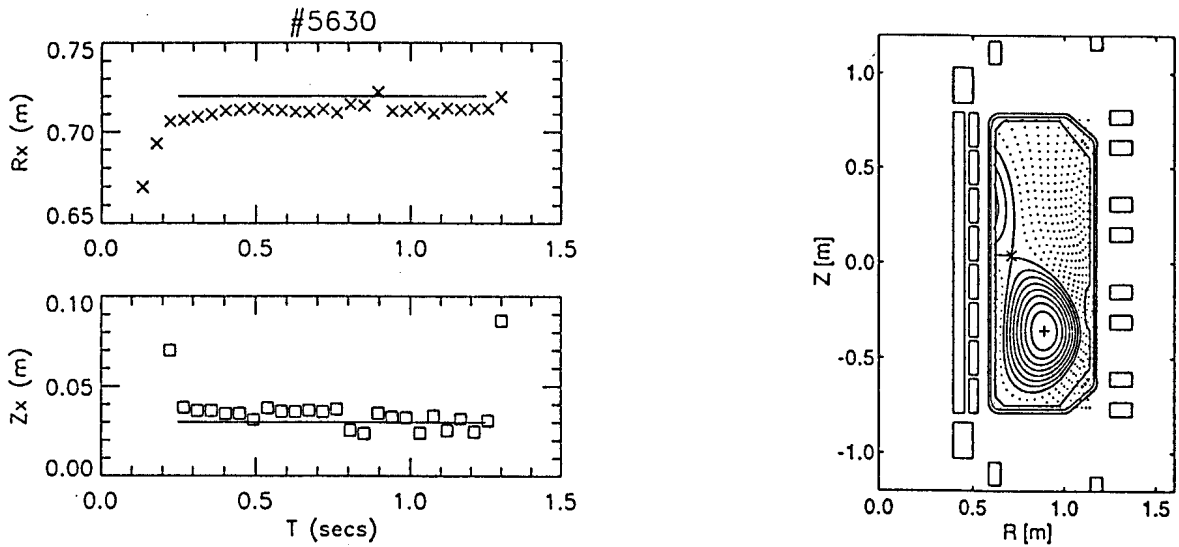


Figure 2. (a) Preprogrammed (lines) and measured (symbols) X-point coordinates for SNX discharge with  $I_p(\text{max})=330\text{kA}$  (b) Magnetic configuration at  $t=0.5\text{sec}$ .

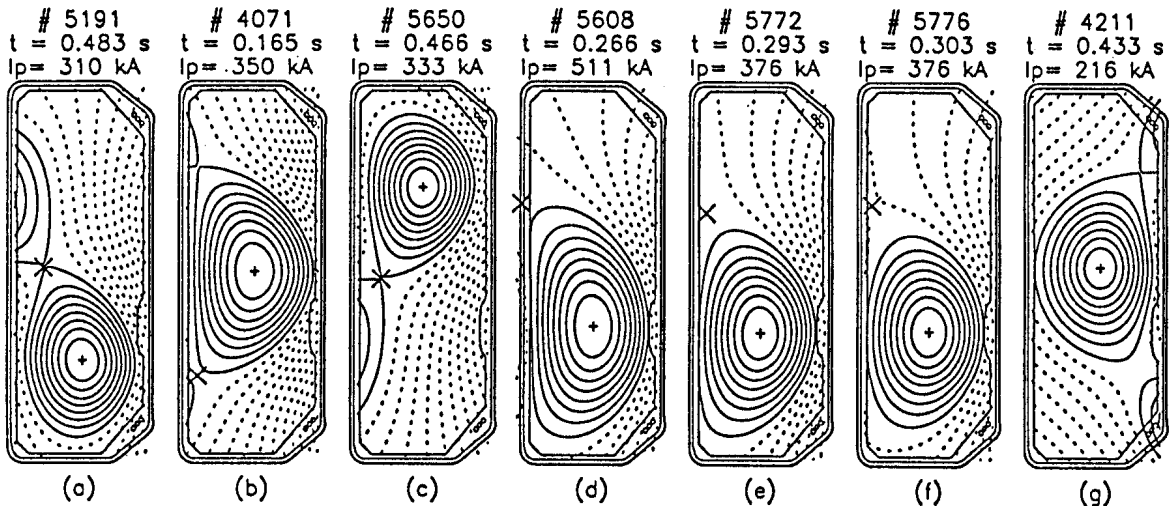


Figure 3. Various plasma shapes produced in TCV

measured shape parameters for a typical limiter discharge. The measured shape parameters were obtained from a full equilibrium reconstruction [11], performed after the discharge. In a second example, figure 2 compares the preprogrammed and measured X-point coordinates of a typical diverted plasma. The shape control algorithm has been tested on a large variety of different configurations. Figures 3a-3g show a selection of equilibrium reconstructions of plasmas that have been produced in TCV.

### 3. Vertical Stability

One of the aims of TCV is to produce plasmas with very high elongation ( $\kappa \leq 3$ ) which are highly unstable with respect to  $n=0$  modes. These modes have been studied by many authors [12-17], and calculations for TCV [16,17] have been performed with the NOVA-W code [18], which includes effects of passive and active feedback elements, as well as plasma deformability. Figure 4 shows some typical results of such calculations with the open-loop growth rate of D-shaped plasmas in TCV shown as a function of elongation ( $\kappa$ ). For  $\kappa=2$ , the equilibrium parameters are those obtained experimentally and for higher values of  $\kappa$ , the plasma current is assumed to increase linearly with elongation and  $q_0$  and  $\beta_p$  to remain constant. In addition, the plasma vertical position is adjusted such that the minimum distance between the plasma boundary and the vacuum vessel floor remains constant. The growth rate saturates above  $\kappa=2.9$ , due to the additional stabilization from the top wall. A comparison between theoretical and experimental growth rates for a plasma with  $I_p=260\text{kA}$ ,  $\kappa=1.6$ ,  $\delta=0.2$  and  $Z_0=-0.23\text{m}$  shows agreement to within 20%.

TCV is equipped with sixteen shaping coils driven independently by thyristor controlled power supplies with a response time of the order of 1 ms. Any combination of shaping coils can be used for vertical position control. However, if the growth rates of highly elongated TCV plasmas (figure 4) are compared with the response time of the shaping power supplies, it is clear that the plasmas with maximum elongation cannot be stabilized using the shaping coils alone. Therefore, it is planned to install a set of internal coils driven by a fast power supply, with a response time of the order of 0.1 ms. Theoretical calculations [16] show that using these fast coils, in combination with the slower shaping coils, should allow the stabilization of growth rates of the order of  $2500\text{ sec}^{-1}$ .

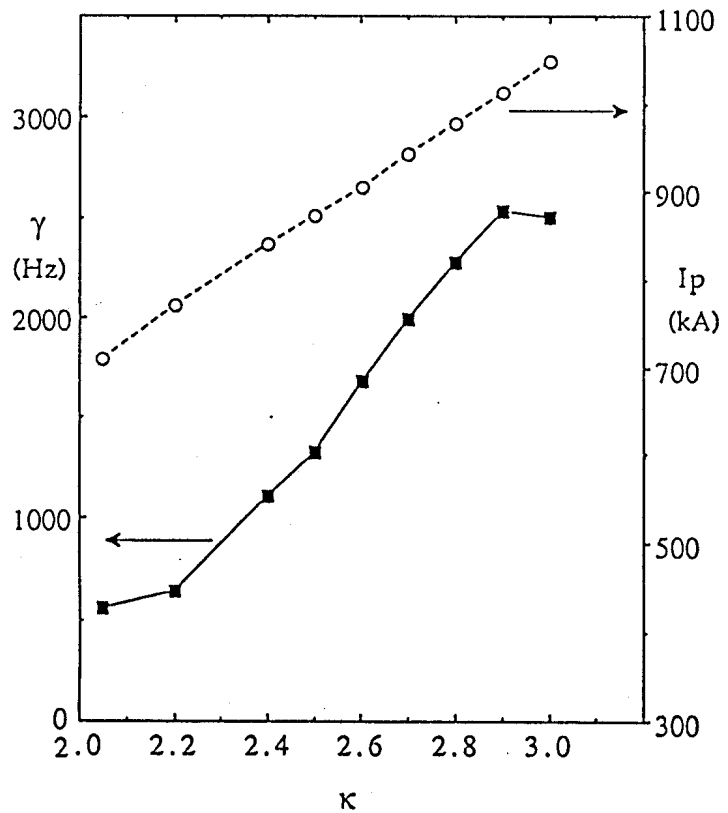


Figure 4. Theoretical growth rate of vertical instability ( $\gamma$ ) and plasma current ( $I_p$ ) vs. elongation for D-shaped plasmas in TCV.

Several experiments have been performed on TCV to determine the maximum vertical growth rate that can be stabilized with the present system. No definitive value has yet been obtained since there are many different ways to measure vertical position and to configure the feedback system, and the optimum choice depends on the plasma configuration being considered. In one particular set of experiments, using four outboard coils for vertical position and velocity control, open-loop growth rates up to  $\gamma=800 \text{ sec}^{-1}$  were stabilized for elliptical plasmas. Since the  $m=1$  shell time,  $\gamma_s^{-1}$ , is 8.2ms in TCV, this corresponds to a stability margin,  $f = (\gamma_s/\gamma)+1 = 1.15$ . This is not a particularly low value since other machines have operated with much lower values of  $f$  [15]. However, the open-loop growth rate in our experiments ( $800 \text{ sec}^{-1}$ ) is close to the inverse response time of the power supplies, so we are probably not far from the limit of what is presently possible in TCV. From the theoretical results in figure 4, the present restriction on the vertical growth rate imposes a limit on the attainable elongation and plasma current.

#### 4. Ohmic H-Mode

Before boronization of the TCV vacuum vessel, experiments with a single null X-point were performed to investigate whether an H-mode could be achieved in deuterium discharges. Since other experiments [19-22] have shown that an ohmic H-mode has a small operational parameter space, the initial experiments were designed to optimize a possible H-mode transition. The X-point was placed near the inner midpoint of the TCV vessel with a distance of more than 2.5 cm between the last closed flux surface and the graphite tiles of the inner wall and the outer belt limiter (figure 3a). The field directions were chosen such that the ion grad B drift was towards the X-point, which was previously found to be more favorable [23]. In order to maximize the ohmic power input, the nominal toroidal field (1.4T) was chosen with a 310 kA plasma current and a modest elongation,  $\kappa_{95}=1.5$ , which corresponds to a safety factor  $q_{95}=2.3$ .

During these initial experiments, distinct evidence of an H-mode type transition was noted in several discharges - a sharp drop in the divertor  $D_\alpha$  signal coincident with a drop in the plasma loop volts and a slight increase in global energy confinement. These features were often triggered by a double sawtooth and appeared both during current ramp-up and plateau phases at a relatively constant line averaged plasma density of  $\langle n_e \rangle = 4 \times 10^{19} \text{ m}^{-3}$ . In the short period between these preliminary observations and the first boronization of TCV, diverted discharges with magnetic configurations shown in figures 3a and 2b showed no further H-mode activity. These experiments were accompanied by a continuous increase in the divertor  $D_\alpha$  signals and hence edge recycling, which appeared to prevent the H-mode transition.

Following boronization, some H-mode activity was again observed and, after a 30 min glow in Helium, sustained ohmic H-modes lasting up to 1 sec were obtained with the configuration shown in figure 2b. In these discharges (figures 5 and 6), there was clear evidence of a density threshold for the H-mode transition. As the plasma density was increased, there was often a short dithering period, followed by the H-mode transition and an ELM-free period. In discharges where large ELMs halted the density rise, and the gas puff was moderate, transition from H back to L mode was achieved without a disruption (figure 5). In cases where no ELMs were observed, the discharge terminated with a high density disruption (figure 6). The maximum line-averaged electron density measured in ELM-free H-modes (configuration figure 2b) was  $1.5 \times 10^{20} \text{ m}^{-3}$ , corresponding to 80% of the Greenwald limit,  $\langle n_e \rangle_{GL} = 0.27 I_p / a^2$  [24].



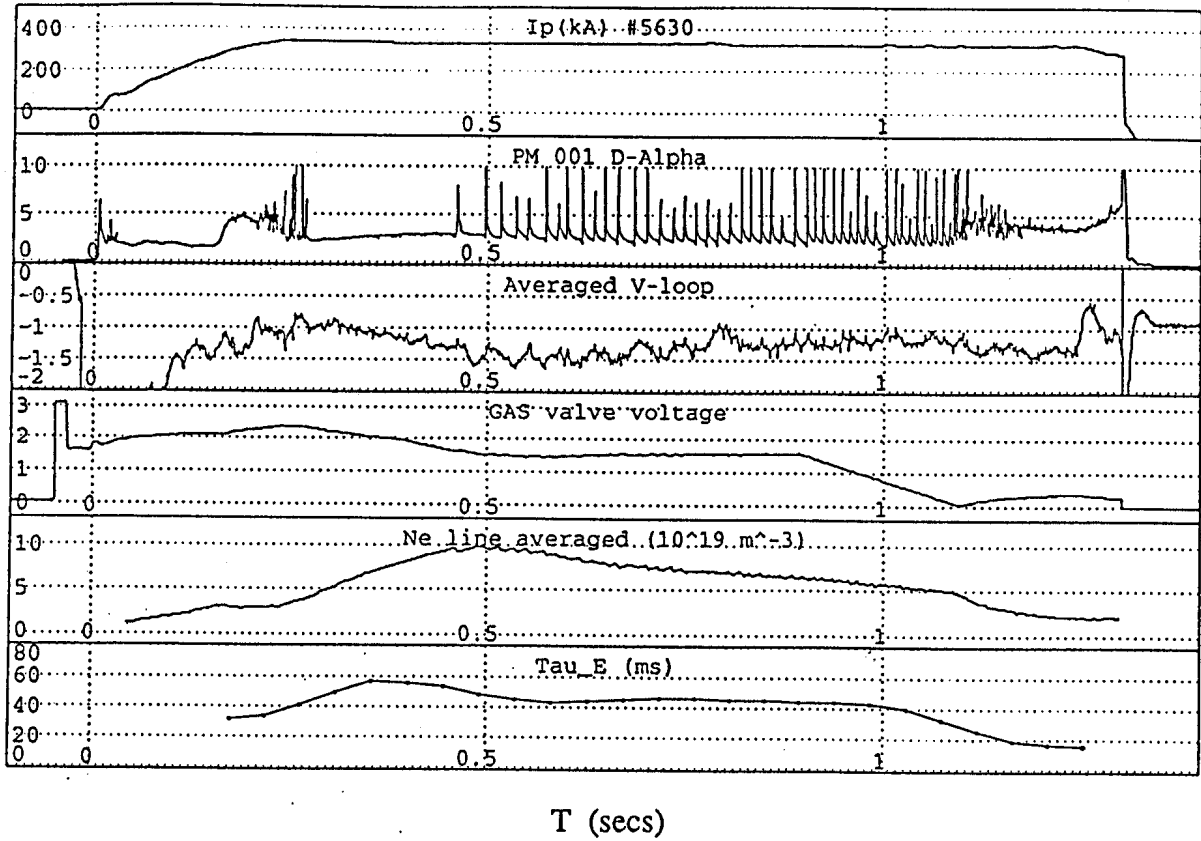


Figure 5. ELMy H-mode discharge (configuration figure 2b)

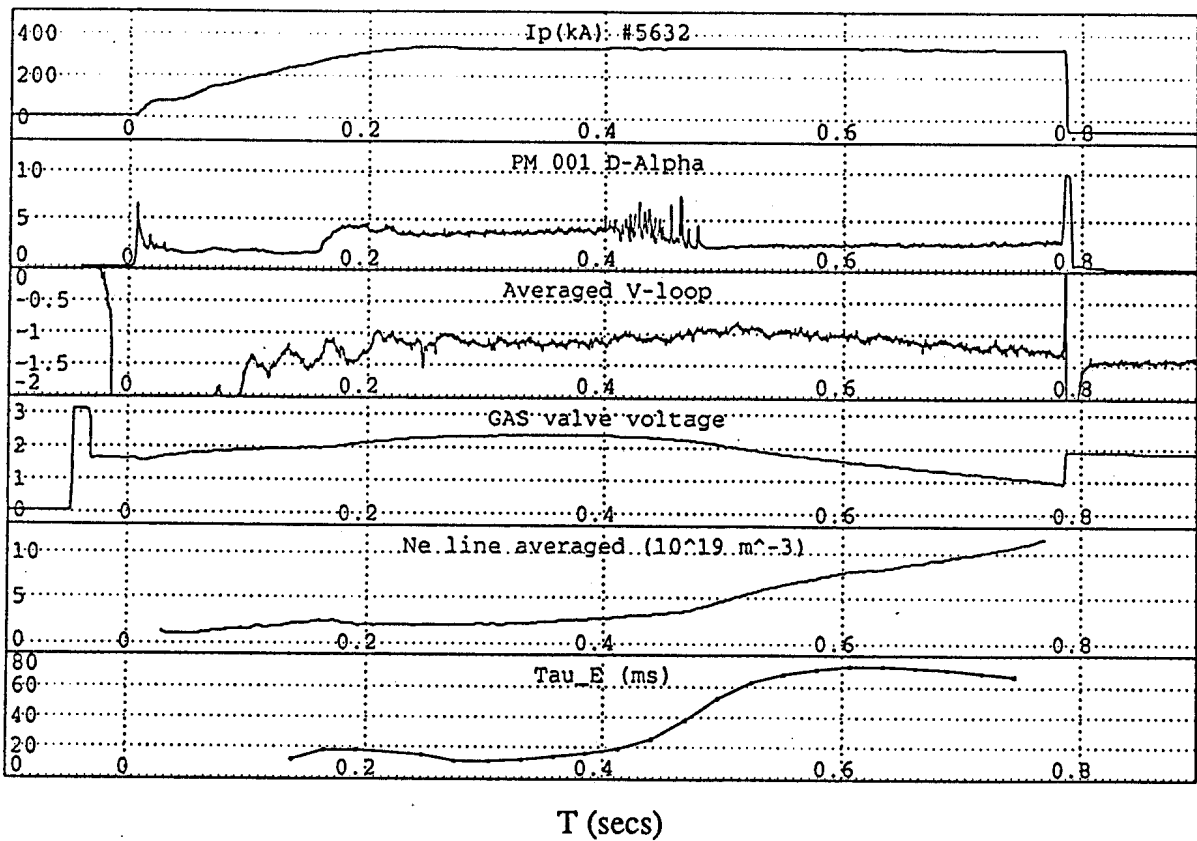


Figure 6. ELM-free H-mode with late L-H transition due to low initial density.

In order to determine the power threshold for the H-mode transition, a plasma current scan was performed with the magnetic configuration shown in figure 2b, at constant toroidal magnetic field, corresponding to a scan of  $q_{95}$  from 2.1 at 340kA to 3.2 at 210 kA. Previous results have shown the required ohmic H-transition power per unit plasma surface area to scale with the product of toroidal field and line averaged plasma density [19]. The current scan gave a threshold for H-mode between 210kA and 240kA, which when compared with other machines [19-22] shows that TCV has easy access to the H-regime with relatively low input power. The H-transition was indeed found to occur at a relatively constant plasma density for each plasma current, which is well demonstrated in figure 5. Here, the initial L-H transition occurs at the same density as the final H-L transition, when the density drops below the critical value of  $4 \times 10^{19} \text{ m}^{-3}$ . We also observed in these experiments that the critical density for the L-H transition is slightly higher when the transition occurs late in the discharge.

To investigate the importance of the ion drift direction, the configuration shown in figure 2b was inverted, maintaining the direction of  $B_{\text{tor}}$  (figure 3c). Operation with a plasma current of 330kA indeed showed some evidence of an H-mode transition at a plasma density very similar to that for the transition observed in the original configuration (figure 2b) at this current. In this case, the density rise following the transition saturated before there was clear ELM activity. Since a further He glow did not improve this H-mode, we conclude that the power threshold in the configuration with the ion grad B drift away from the X-point is at least 50% higher than with the ion drift towards the X-point.

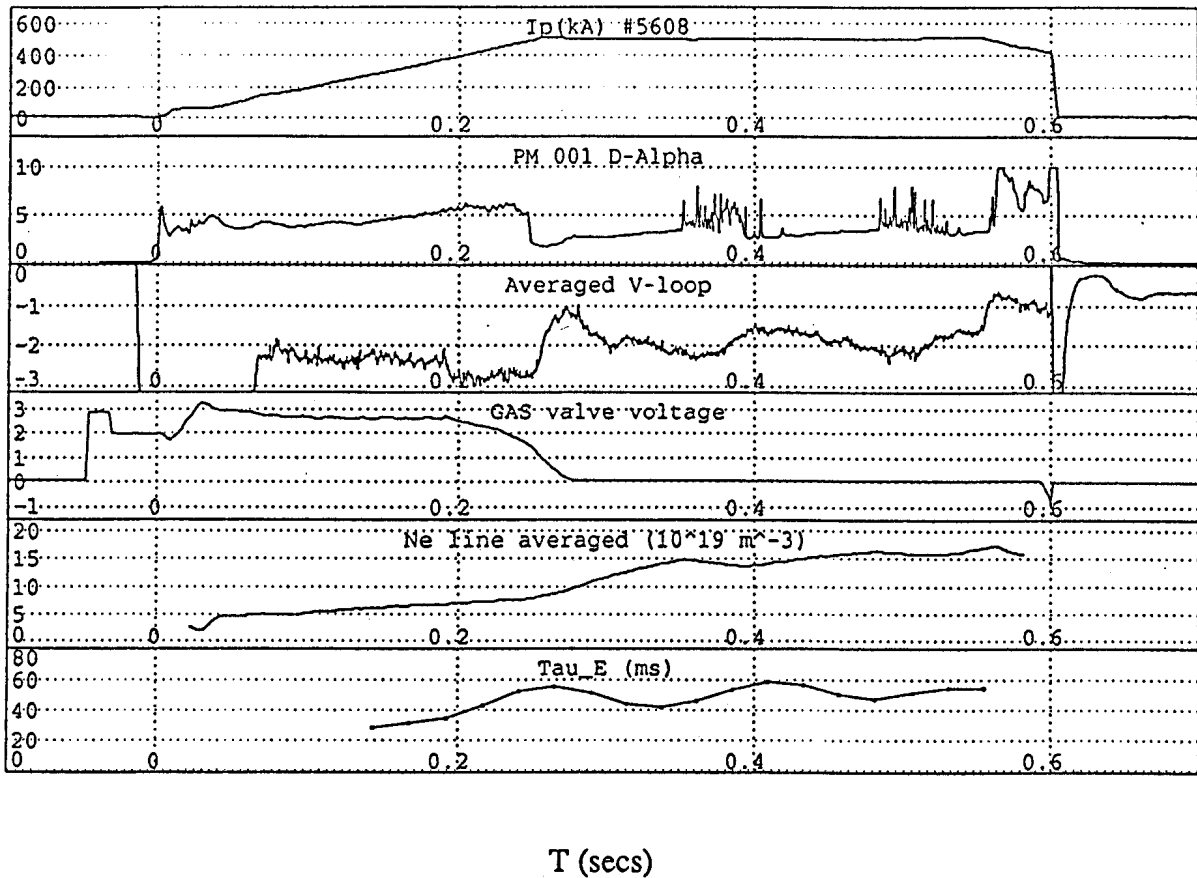


Figure 7. H-mode in D-shaped limiter plasma (configuration figure 3d)

The density limit, following boronization of the vessel, is often used as a measure of the "quality" of the wall boronization. Although little deterioration was observed in the density limit, measured from the high density disruptions during ELM free operation, it became impossible to avoid long ELM-free discharges which inevitably terminated with a density disruption. A 30min Helium glow immediately restored the large ELM activity, stabilizing the density rise during the H-mode phase.

The importance of high density for the ohmic H-mode in TCV was unexpectedly demonstrated in a series of limiter discharges with high elongation ( $\kappa=1.9$ ) and plasma currents up to 600kA (e.g. figure 3d with  $I_p=510\text{kA}$ ). As the density was raised by gas puffing, the discharge went into H-mode at fairly reproducible plasma density ( $\langle n \rangle = 8 \times 10^{19} \text{ m}^{-3}$ ) and there were ELM-free and large ELM periods (figure 7). The maximum line averaged electron density reached in these limiter discharges was  $1.7 \times 10^{20} \text{ m}^{-3}$  and although some discharges showed several L-H and H-L transitions, all terminated in a major disruption. The magnetic configuration was nearly up-down symmetric with two X-points located close to the vessel wall (figure 3d). The distance between the X-points and the plasma boundary was 9 cm and the poloidal flux difference between the X-point and the limiter surface was 4% of the total poloidal flux within the plasma. This leads to an extremely wide interaction zone of the scrape off layer with the carbon tiles, which may explain the access to a limiter H-mode in TCV.

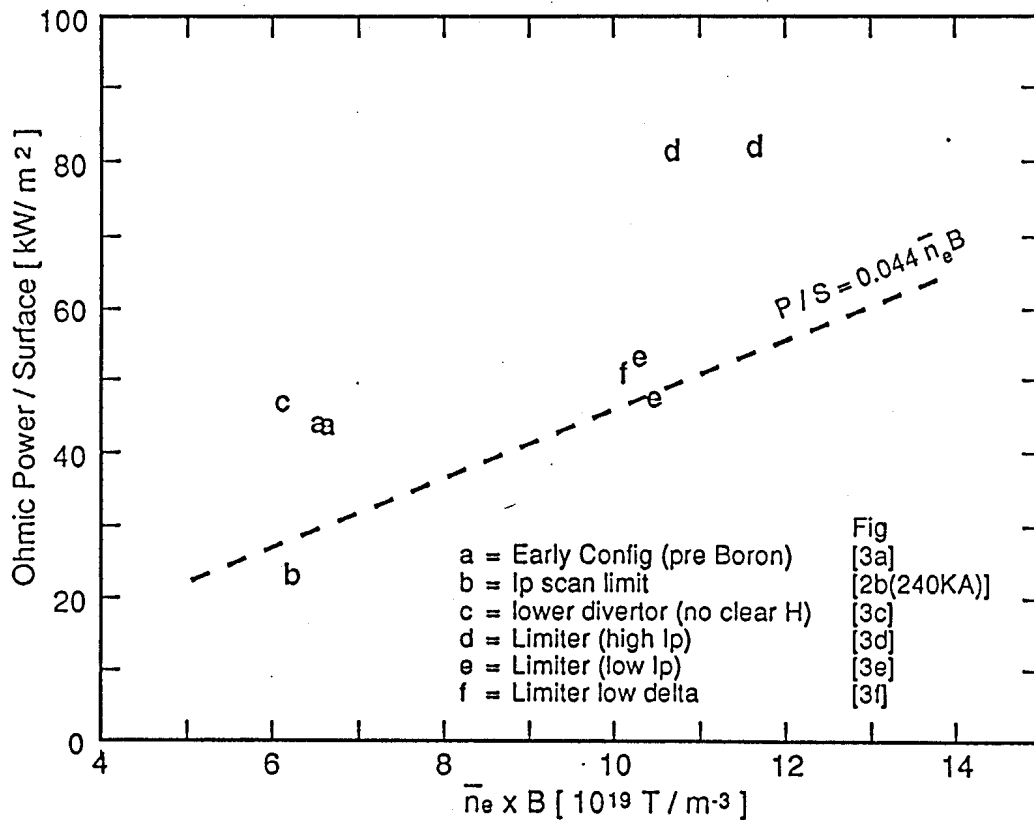


Figure 8. Ohmic power divided by the area of the last closed flux surface vs.  $n_e B$  for L-H transitions in TCV. Dashed line is scaling from Ref. [19].

In these experiments the power threshold for the limiter H-mode depended on the plasma triangularity. A discharge with  $I_p=370\text{kA}$ ,  $\kappa=1.7$ ,  $\delta=0.4$  (figure 3e) showed reproducible L-H transitions at line-averaged densities around  $7 \times 10^{19} \text{ m}^{-3}$ . When the triangularity was decreased to  $\delta=0.25$  (figure 3f), the transition no longer occurred, but

with a slightly larger plasma current,  $I_p=400\text{kA}$ , the limiter H-mode reappeared. This may be explained by the fact that the distance between the X-point and the plasma boundary increases with decreasing triangularity. In figure 3f, this distance is quite large (17 cm), and the flux between the X-point and the limiter surface amounts to 12% of the total plasma flux. Yet, this configuration (with  $I_p=400\text{kA}$ ) showed a clear L-H transition at  $\langle n_e \rangle = 7.2 \times 10^{19} \text{m}^{-3}$ . A summary of the threshold conditions for the ohmic H-mode in TCV is shown in figure 8 and compared with the scaling law given in Ref. [19].

### 5. Energy Confinement Time

In this section, we present a preliminary analysis of the energy confinement time in L and H-mode discharges. Since electron density and temperature profiles are only available for a small fraction of the discharges [1] and ion temperatures are not yet measured,  $\tau_E$  is derived from equilibrium reconstructions [11], based on magnetic measurements. The energy confinement time is calculated as  $\tau_E = W / (I V_1 - dW/dt - dU/dt)$ , where  $W$  is the plasma thermal energy,  $W = (3/2) \int p dV$ ,  $V_1$  is the loop voltage evaluated on the last closed flux surface, and  $U$  is the internal poloidal magnetic field energy,  $U = (\mu_0/4) I_p^2 R_i$ .

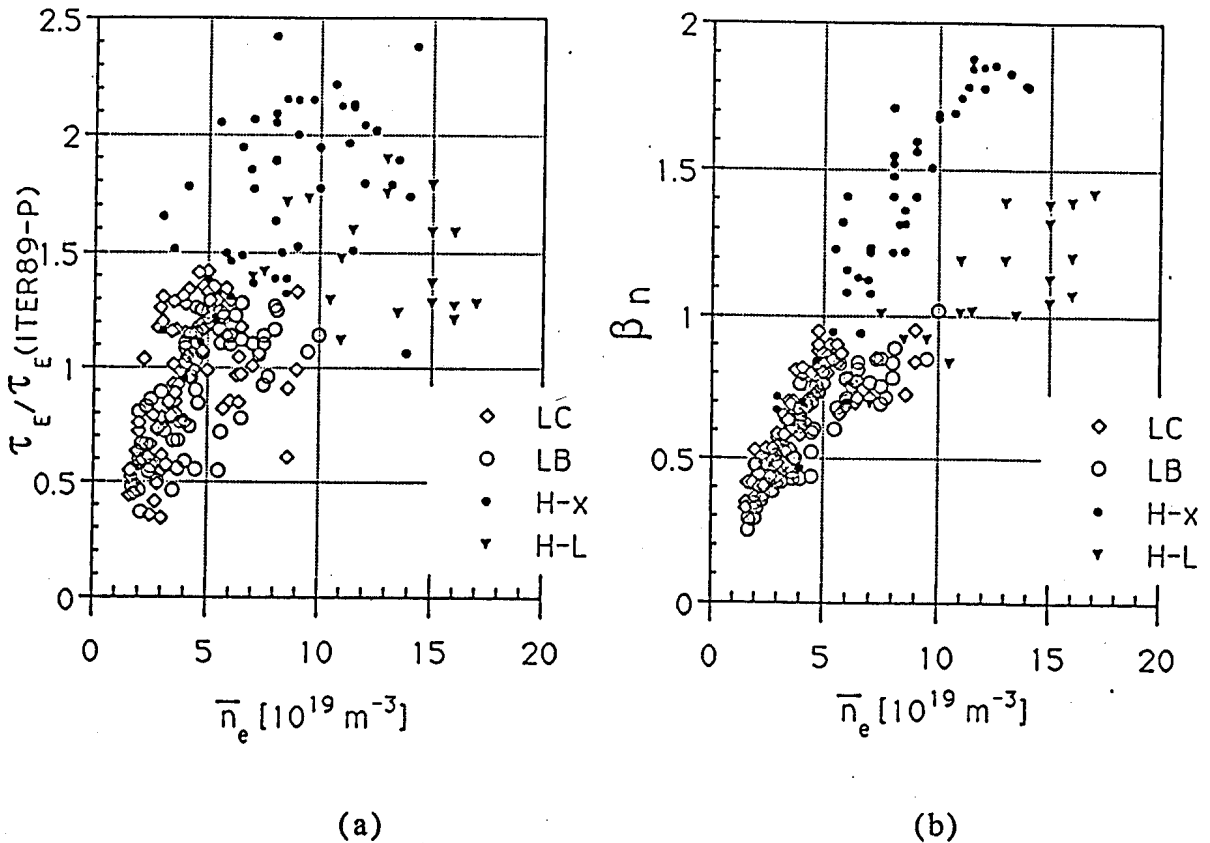


Figure 9. Enhancement of energy confinement time with respect to ITER89-P (a) and normalized beta (b) vs. line averaged electron density, for L-mode discharges in unboronized (LC) and boronized vessel (LB) and for H-mode discharges with single-null X-point (H-X) and limiter configuration (H-L).

In figure 9a, the enhancement of the energy confinement time with respect to ITER89-P scaling is shown as a function of line averaged electron density for four different types of discharges. The plot includes plasmas within the following parameter ranges:  $250\text{kA} < I_p < 800\text{kA}$ ,  $1.2 < \kappa < 2.05$ ,  $0.1 < \delta < 0.5$ ,  $2.1 < q_{95} < 4.5$ , and  $1.0 < B_p < 1.46\text{T}$ . The TCV database is currently too sparse to provide a definite dependence<sup>tor</sup> of  $\tau_E$  on plasma shape and current. In L-mode, the maximum enhancement in  $\tau_E$  increases until  $\langle n \rangle \sim 5 \times 10^{19} \text{m}^{-3}$  and stays at this value for higher  $\langle n \rangle$ . This dependence did not change significantly with boronization. In contrast, for H-modes with a single-null X-point configuration, the enhancement in  $\tau_E$  increases up to  $\langle n \rangle \sim 1 \times 10^{20} \text{m}^{-3}$  and then decreases. The maximum energy confinement time obtained in an ELM-free H-mode was 80ms, corresponding to an enhancement factor of 2.4. In limiter H-modes, the enhancement in  $\tau_E$  also increases with  $\langle n \rangle$ , but the values are considerably lower than in divertor configurations. Figure 9b shows a plot of normalized beta,  $\beta_N = (\beta_{\text{tor}} [\%] a [\text{m}] B [\text{T}] / I_p [\text{MA}])$ . The H-modes reach much higher  $\beta_N$ -values than L-modes, and the maximum values obtained in single-null X-point configurations are about a factor of 1.4 above those observed in limiter H-modes.

## 6. Conclusion

Using a novel shape control algorithm [9], TCV has produced plasmas with various shapes and magnetic configurations, characterized by  $1.0 \leq B_p \leq 1.46\text{T}$ ,  $I_p \leq 800\text{kA}$ ,  $\kappa \leq 2.05$ ,  $\delta \leq 0.7$ . The optimization of the vertical position control<sup>tor</sup> system has allowed the stabilization of vertical growth rates up to  $800 \text{sec}^{-1}$ , which is close to the inverse of the response time of the power supplies.

Experiments with a single-null X-point and plasma currents between 210kA and 340kA showed that TCV has easy access to the ohmic H-mode if the ion grad B drift is directed towards the X-point, and if the vessel is boronized and conditioned with helium glow discharges. ELMy and ELM-free H-modes, lasting for 1.0sec and 0.4sec, respectively, have been obtained. Energy confinement times of 80ms, normalized beta ( $\beta_{\text{tor}} a B / I_p$ ) of 1.9 and  $\tau_E$  enhancement ( $\tau_E / \text{ITER89-P}$ ) of 2.4 have been observed in ELM-free ohmic H-modes. The L-H transition is observed to occur at a constant density for each combination of plasma current and magnetic configuration. Reversing the direction of the ion grad B drift prevented the appearance of the ohmic H-mode, even with an input power corresponding to 150% of the threshold power observed in the original configuration.

Limiter H-modes have been obtained in D-shaped plasmas with  $360\text{kA} \leq I_p \leq 600\text{kA}$ ,  $1.7 \leq \kappa \leq 1.9$ . The density threshold for the limiter H-mode transition is considerably higher than that found in the single-null X-point configuration, and the power threshold is found to increase with decreasing triangularity.

## Acknowledgements

It is a pleasure to acknowledge the support of the TCV technical teams throughout the first experimental campaigns. This work was partially supported by the Swiss National Science Foundation.

## References

- [1] Behn, R., Pietrzyk, Z.A., Franke, S, this Conference.
- [2] Nieswand, C., Behn, R., Bühlmann, F., et al., this Conference.
- [3] O'Brien, D.P., Ellis, J.J., Lingertat, J., Nuclear Fusion 33 (1993) 467.
- [4] Campbell, G.L., Ferron, J.R., McKee, E., et al. FUSION TECHNOLOGY 1992, Elsevier Science Publishers 2 (1993) 1017.
- [5] Bell, R.E., Asakura, N., Bernabei, S., et al. Phys. Fluids B 2 (1990) 1271.
- [6] Todd, T.N., and COMPASS Team, Plasma Phys. and Controlled Fusion 35 (1993) B231.
- [7] Lister, J.B., Schnurrenberger, H., Nuclear Fusion 31 (1991) 1291.
- [8] McCarthy, P.J., Schneider, W., et al., Proc. 19th EPS Conf. on Controlled Fusion and Plasma Physics, 16C, I, 459.
- [9] Hofmann, F., Jardin, S.C., Nuclear Fusion 30 (1990) 2013.
- [10] Hofmann, F., Tonetti, G., Nuclear Fusion 28 (1988) 519.
- [11] Hofmann, F., Tonetti, G., Nuclear Fusion 28 (1988) 1871.
- [12] Perrone, M.R., Wesson, J.A., Nuclear Fusion 21 (1981) 871.
- [13] Ward, D.J., Jardin, S.C., Nuclear Fusion 32 (1992) 973.
- [14] Hutchinson, I.H., Nuclear Fusion 29 (1989) 2107.
- [15] Lister, J.B., Lazarus, E.A., Kellman, A.G., et al. Nuclear Fusion 30 (1990) 2349.
- [16] Ward, D.J., Hofmann, F., Nuclear Fusion 34 (1994) 401.
- [17] Ward, D.J., Bondeson, A., Hofmann, F., Nuclear Fusion 33 (1993) 821.
- [18] Ward, D.J., Jardin, S.C., and Cheng, C.Z., J. Comput. Phys. 104 (1993) 221.
- [19] Ryter, F., Gruber, O., Büchl, K., et al., in Controlled Fusion and Plasma Physics (Proc.. 20th Eur. Conf. Lisboa, 1993), Vol 17C, Part I, European Physical Society (1993) I-23.
- [20] Osborne, T.H., Brooks, N.H., Burrell, K.H., et al., Nuclear Fusion 30 (1990) 2023.
- [21] Snipes, J.A., Granetz, R.S., Greenwald, M., submitted for publication in Nuclear Fusion.
- [22] Carolan, P.G., Fielding, S.J., Gerasimov, S., et al, to be published in Plasma Physics and Controlled Fusion.
- [23] ASDEX Team, Nuclear Fusion 29 (1989) 1959.
- [24] Greenwald, M., et al. PFC/JA-86-22, Plasma Fusion Center, MIT, Cambridge, Mass., U.S.A.

## The Thomson Scattering Diagnostic on the TCV Tokamak

**R. Behn, S. Franke, Z.A. Pietrzyk**  
*Association Euratom - Confédération Suisse*  
*Centre de Recherches en Physique des Plasmas*  
*Ecole Polytechnique Fédérale de Lausanne*

The TCV tokamak has been designed to offer large flexibility in the generation of plasma configurations with different shapes. In particular plasmas with highly elongated poloidal cross sections will be studied. These boundary conditions have influenced the design of the Thomson scattering system. When fully implemented this diagnostic will comprise 2 independent systems for observation along a vertical and a horizontal laser beam path. At present we have installed a basic version of the system using the vertical chord. Good access via 3 horizontal ports (in one toroidal sector) will give us view over the full height of the vacuum vessel (approx. 1.3m) including the zones where the X-points of divertor plasmas will be formed. So far measurements are limited to 10 observation points, which have been arranged to cover the lower half of the vessel (from  $z = -.55$  to  $+.21$ m, spatial resolution  $\Delta z = 35$ mm).

Using a repetitively pulsed Nd:YAG laser operated at 20Hz we can follow the temporal evolution of electron temperature and density during tokamak discharges, which can reach durations of about 2s in the case of TCV. The lasers are located in a separate room outside the tokamak safety area. An air-tight beam duct comprising several folding mirrors is used for transfer of the laser beam over a total distance of 20m. The overall transmission of the system is better than 80%.

The scattered light collected by one of the wide angle lenses ( $F\text{-}\# = 2$ ) is focused onto optical fiber bundles (max. 11 for each lens assembly) and transmitted to polychromators for spectral analysis in 3 channels on the short wavelength side of the spectrum. We use sets of interference filters with pass bands that have been optimized for operation over a  $T_e$  range from 50 to 2000eV. Low F-number optics are required to match the numerical aperture ( $N.A. = 0.22$ ) of the optical fibers. Si-avalanche photodiodes are used as detectors offering good quantum efficiency up to 1000nm and sufficient internal gain for low level light detection. After further amplification the signals are sent to a data acquisition unit consisting of CAMAC modules (LeCroy FERA gated integrators and buffer memory).

Assuming a Maxwellian velocity distribution the electron temperature  $T_e$  can be obtained from the ratios of the signals recorded in different polychromator channels. This simple and fast procedure has already been adapted successfully in the past [1,2] and has the advantage to produce results almost immediately after each shot. Once  $T_e$  is known  $N_e$  can be evaluated from the signal amplitude in one of the channels whose sensitivity has to be determined by an absolute calibration method. We use Raman scattering in  $N_2$  gas for this purpose [3].

- |     |                              |                                    |
|-----|------------------------------|------------------------------------|
| [1] | J. Lasalle, P. Platz         | Appl. Opt. <b>18</b> , 4124 (1979) |
| [2] | H. Röhr, K.-H. Steuer et al. | Nucl. Fus. <b>22</b> , 1099 (1982) |
| [3] | J. Howard, B.W. James et al. | J. Phys. D <b>12</b> , 1435 (1979) |
| [4] | Chr. Nieswand et al.         | poster D-34 at this conference     |

The system has been installed on the TCV tokamak at the beginning of 1994 and is now producing data on a regular basis. So far the effort has been concentrated on testing its performance and reliability. The optical system has proven to be stable over periods of several months without any need for realignment. Raman calibration measurements have shown that the stray light level is extremely low and the sensitivity good enough to permit measurements down to  $N_e=10^{18}m^{-3}$ . We have chosen to present here only some recent results for which our latest Raman calibration is still applicable.

The first example (TCV shot # 5769) shows data of a limiter plasma at moderate current ( $I_{pmax}$  260 kA) and elongation ( $\kappa=1.5$ ) with a constant line-integrated density during the current plateau. Sawtooth activity is observed during most of the discharge duration (see fig. 1). The plasma is centered in the lower half of the vessel where most of our observation points are located (see fig. 2). Fig. 3 shows the spatial profiles of  $T_e$  and  $N_e$  at 5 different time steps during the density plateau. The marker bar indicates the location of the magnetic axis as obtained from an equilibrium reconstruction code. From the measured density profile and reconstruction data we have evaluated the line integrated density, which can then be compared to measurements from the FIR interferometer [4]. The agreement is within 20% which is acceptable given the limited number of data points on our density profiles. As a second example (TCV shot # 5790) we show measurements during a controlled vertical displacement of an elongated plasma. In this case the plasma column was shifted by about 100mm after the current plateau has been reached (see fig. 4). The sampling rate of 20 Hz determined by the YAG laser was well adapted to follow the dynamic behavior of the  $T_e$  and  $N_e$  (fig.5). Fig. 6 shows  $T_e$  and  $N_e$  profiles at 3 time steps; although the profiles are not perfectly symmetric they clearly follow the displacement of the magnetic axis.

These examples demonstrate the capabilities of the system but they also show its present limitations due to the restriction to 10 observation points, which are not always well placed for the particular plasma configuration to be studied. Therefore we envisage an upgrade to a total of 30 points in the near future. The collection optics on 3 ports is already in place such that complete vertical profiles can be obtained as soon as the additional equipment (polychromators etc.) becomes available. Further improvements, especially as far as spatial resolution near the plasma boundary is concerned, are expected from the horizontal beam system. Due to the special geometry of this configuration - the laser beam is almost tangential to the flux surfaces near the inner boundary - the radial resolution will be of the order of 5mm. We also intend to combine the beams of up to 4 lasers along a single cord in such a way that the scattering volumes will be inside the depth of field of the collection optics. This configuration will offer improved flexibility in the timing sequence of the measurements, since each laser can be triggered independently using a computer controlled timing system.

This work was partially funded by the Swiss National Science Foundation.



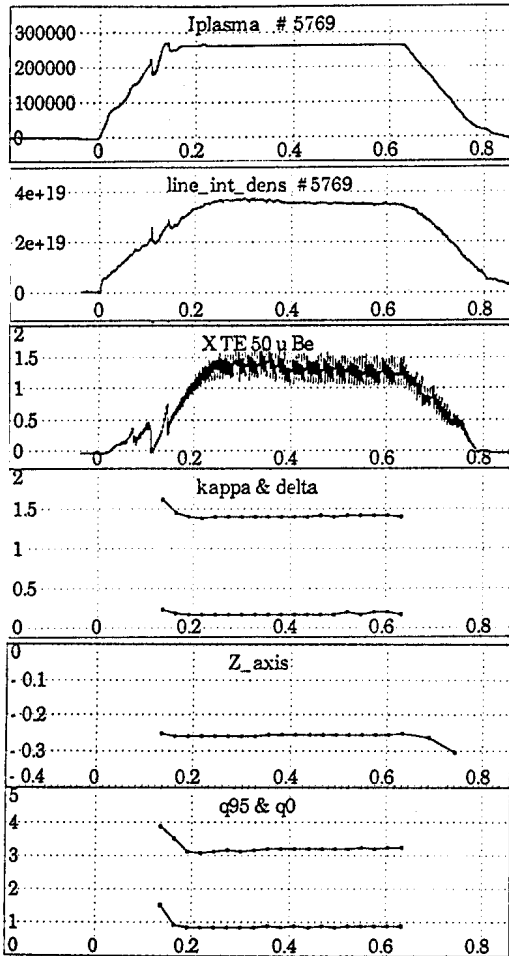


**Fig. 1**  
History of TCV shot # 5769

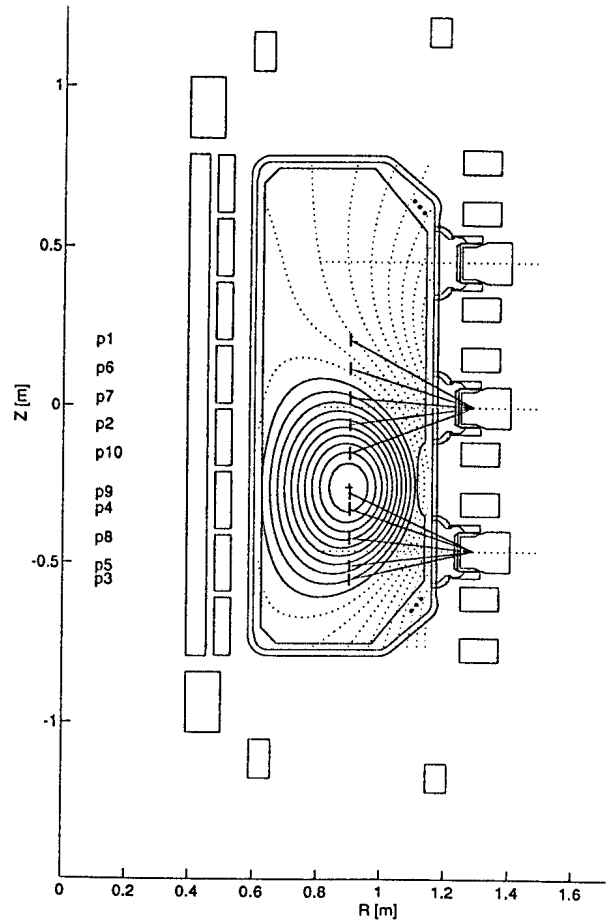


**Fig. 2**  
Poloidal cross section of the TCV tokamak showing reconstructed flux surfaces for shot # 5769, at  $t=0.4$  s, together with 10 observation points of the Thomson scattering system.

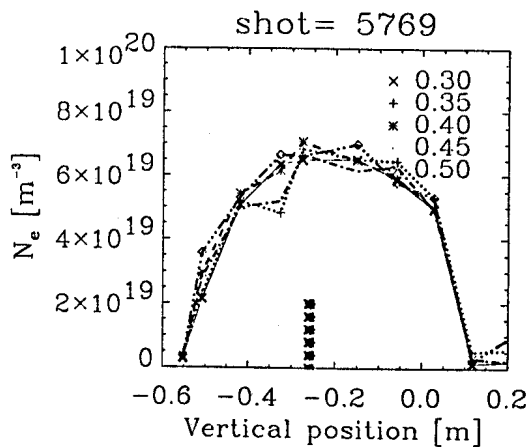
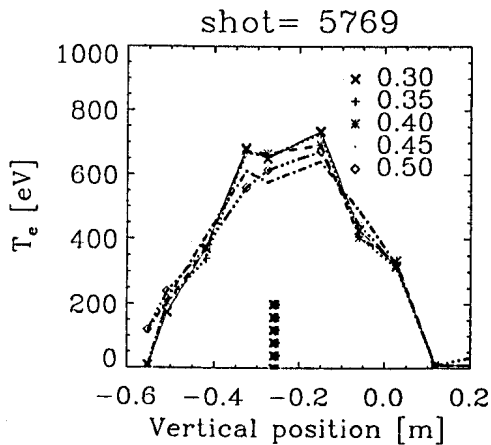


**Fig. 3**  
Spatial profiles along  $z$  of  $T_e$  and  $N_e$  for TCV shot # 5769 at time steps [ 0.3 , 0.35 , 0.4 , 0.45 , 0.5 s ].

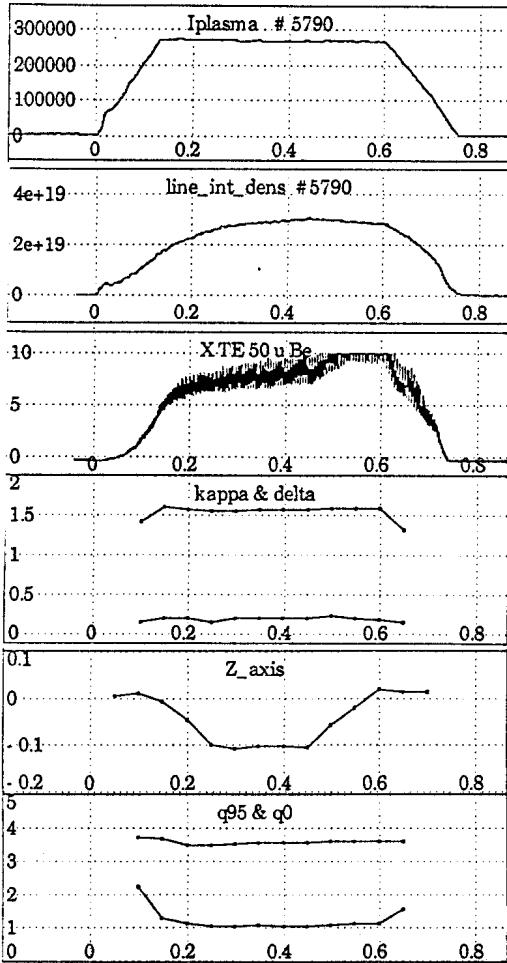


**Fig. 4**  
History of TCV shot # 5790  
(controlled vertical shift)

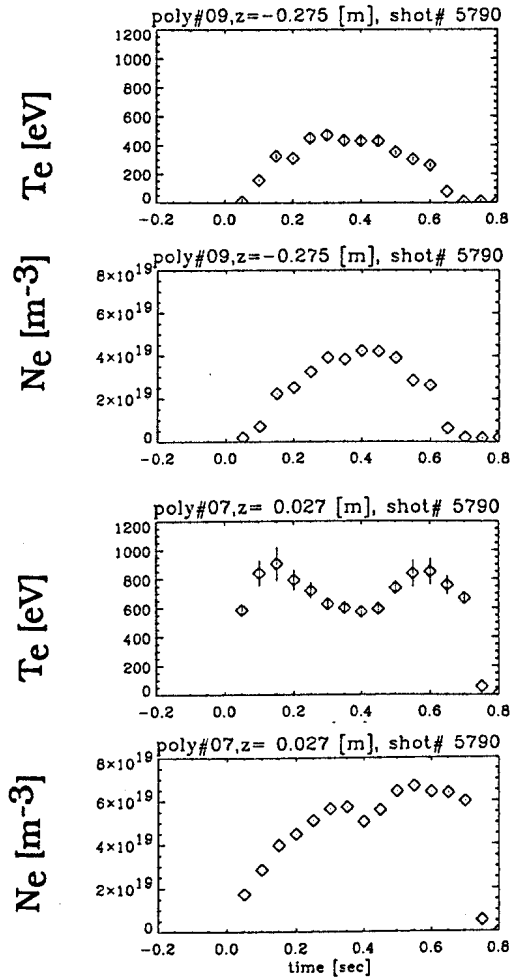


**Fig. 5**  
Time evolution of Te and Ne  
at two z-positions

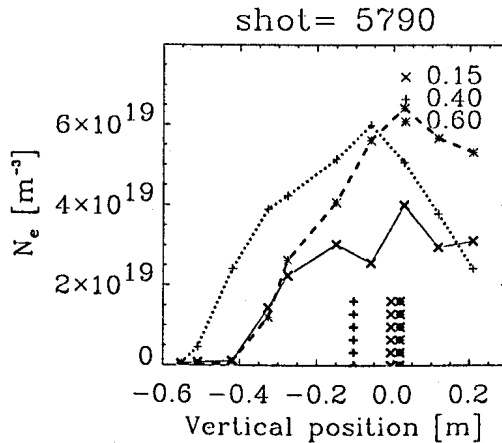
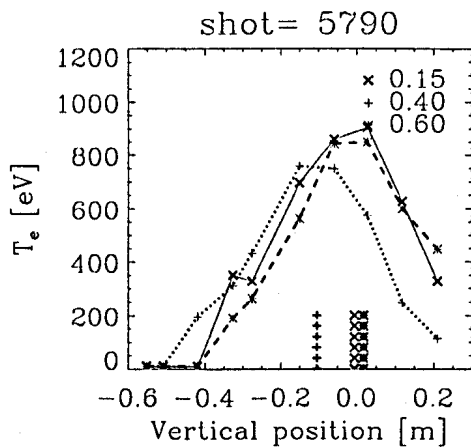


**Fig. 6**  
Spatial profiles of Te and Ne for TCV shot # 5790  
at time steps [ 0.15 , 0.4 , 0.6 s ] ;  
bars mark position of magnetic axis at each time step.

## Experimental Study of Ion Phase Space in the Approach to Large Scale Chaos in Wave-Particle Interaction

**A.F.Fasoli and F.N.Skiff<sup>+</sup>**

*Centre de Recherches en Physique des Plasmas*

*Association Euratom-Swiss Confederation*

*Ecole Polytechnique Federale de Lausanne, 21, av. des Bains, CH-1007,*

*Lausanne, Switzerland*

### ***Introduction***

The non-linear regime in wave-particle interaction is recognised to be of great importance both in space and laboratory plasmas. Different natural mechanisms, such as particle precipitation in the ionosphere<sup>1</sup>, are linked to the transition to chaos generated by plasma waves. In fusion relevant plasmas, several applications of chaos can be identified, including stochastic plasma heating<sup>2</sup> and, to quote a recent development, fast particle anomalous transport in the field of one or more global Alfvén Eigenmodes both in tokamaks and stellarators<sup>3</sup>. In the latter case, the presence of more than one mode is predicted to lower the threshold for transition to chaos and therefore to ease the triggering of enhanced losses of fast particles, such as non-thermal alphas in burning plasmas<sup>4</sup>. The transition to chaos in two wave-particle interaction, producing stochastic particle orbits, has been demonstrated experimentally in a linear magnetised plasma<sup>5</sup>. In this paper we shall review the main results illustrating the physics of the transition to chaos, focusing our attention on the reconstruction of ion phase space features, such as local transport coefficients, in the approach to dynamical chaos.

### ***Experimental set-up and diagnostic methods***

The experiments are performed on the CRPP Linear Magnetised Plasma (LMP) Q-device. The plasma is produced by a combination of surface ionisation of barium vapours and thermo-ionic emission from a plate heated by electron bombardment, and is characterised by a high degree of spatial and temporal uniformity. Radial confinement is provided by a solenoidal B-field ( $B \approx 2$  kG). The whole plasma column streams uniformly along the field lines away from the source at supersonic speed ( $v_D \approx 2-3 \times v_{thi}$ ). Typical temperatures and densities are  $T_{i\perp} \approx 2T_{i\parallel} \approx 0.2$  eV and  $n \approx 10^9-10^{10}$  cm<sup>-3</sup>. Electrostatic ion waves are excited by means of four rings encircling the plasma column and fed with different phases by a signal in the ion cyclotron frequency range. A single frequency is placed on the ring antenna in the laboratory frame. The wave frequency in the plasma frame is either up- or down-Doppler shifted according to the direction of propagation along the magnetic field. Waves with two parallel phase velocities, differing roughly by the thermal speed, are observed. The plasma response to these externally excited waves is measured mainly via optical active diagnostic techniques. Laser Induced Fluorescence (LIF) allows a local observation of the space and time resolved distribution function  $f(x, v, t)$ , which in turn embeds information on the wave characteristics. The study of dynamical particle orbits, however, requires us to complement this local, or 'eulerian', approach, with a non-local, or 'lagrangian', description of ion phase

space. This can be achieved through optical tagging of ions, i.e. changing their quantum state density by means of a properly tuned laser beam ('optical pumping'). A test-particle distribution can thus be created and followed in its evolution both in configuration and velocity space. The scheme of optical tagging employed here is based on the spin polarisation of barium ground state ions<sup>6</sup>. Different geometrical arrangements for the tag and detection beam injection allow different phase space quantities to be directly measured or reconstructed. Fig.1 shows a sketch of the LMP apparatus, including the ring antenna, the different injection points for the tag and search beams and the relative fluorescence detector.

### *Experimental results*

Both single particle hamiltonian theories<sup>7</sup> and self-consistent particle simulations<sup>8</sup> predict that in the presence of two waves the plasma particle trajectories can assume a chaotic character for amplitudes exceeding a certain threshold. A stochasticity parameter is usually introduced in the form<sup>7</sup>:  $K=2(A_1^{1/2} + A_2^{1/2})$ , where  $A_i=eV_i/m(\Delta v_\phi)^2$  is the normalised amplitude of the mode  $i$ , with  $V_i$  being the relative wave potential.  $\Delta v_\phi$  is the difference between the two parallel phase velocities.  $K=1$  represents the threshold for the transition to chaos. For  $K>1$  significant particle transport and acceleration should be triggered. Correspondingly, macroscopic fast ion heating should be achieved. Fig.2(a) shows the steady state parallel temperature as a function of the excitation amplitude; a threshold value can be identified, above which a significant heating occurs. The  $K=1$  region, as evaluated from a calibration of the wave amplitude based on the ion dielectric response, corresponds to the shaded area on the amplitude axis. A fast time scale, corresponding to a bulk velocity space diffusion coefficient at least one order of magnitude larger than the collisional one, has also been observed to characterise this heating process. Via a scheme of narrow-band spin state tagging allowing observation of radial transport<sup>9</sup>, the exponential separation of initially close ion trajectories has been demonstrated. The measured exponential divergence rate is in agreement with the calculated Kolmogorov-Sinai entropy<sup>10</sup>. The mechanism for the observed ion heating has therefore been unambiguously identified as wave-induced dynamical chaos. A different tagging experiment, with a pulsed tag beam injected vertically through a cylindrical lens at a specific axial location, is used for reconstructing the parallel ion trajectories. The bandwidth of the tag laser is broad enough to avoid perpendicular velocity selectivity. Conversely, the search laser is injected in parallel to the B-field and does operate a selection within the parallel distribution. By measuring the time of flight for the different final velocity classes, and extrapolating the initial velocity from the average velocity, the correlation between two phase space points  $(v_{\text{initial}}, z_{\text{initial}}) \rightarrow (v_{\text{final}}, z_{\text{final}})$  can be established. From the spread in the time of flight spectra, an evaluation of the diffusion coefficient in velocity space,  $D_{VV} = \langle \delta v \delta v / \delta t \rangle$ , can be obtained. If fig.2(b) we show the diffusion coefficient for the bulk of the distribution, averaged over the wave phase, as a function of the wave excitation amplitude. A sudden increase in  $D_{VV}$  occurs at the threshold for stochastic heating (fig.2a), as expected for a transition in the orbit character from regular to chaotic. At large excitation amplitude, a tendency to saturate is shown

by the experimental curve, in agreement with the macroscopic estimates of  $D_{VV}$  based on the time resolved heating measurements. This saturation of the heating mechanism can be related to changes in the wave spectrum as the chaotic regime is approached, suggesting the presence of self-consistent effects between particle and wave fields. When different final velocity classes are selected by the tunable search laser, the dependence of the  $v$ -space diffusion coefficient upon the velocity can be studied. In fig.3 we report the curves relative to two different wave amplitudes, (a) far below the stochastic threshold ( $K \ll 1$ ) and (b) in the range of the threshold ( $K \sim 1$ ). In Fig.3(a) we see that the diffusion coefficient peaks in correspondence of the two parallel phase velocities ( $v_{\phi 1}$  and  $v_{\phi 2}$ ), indicating a locally wave-enhanced particle transport. When the wave amplitude approaches the stochastic threshold, the  $v$ -space transport appears to be significantly enhanced over large portions of the phase space (Fig.3(b)). By operating the same kind of measurement for a series of initial phases, the ion phase space dynamical flow in the parallel phase space plane can be reconstructed for different wave amplitudes. Structures are observed to appear and evolve on the phase space as the wave amplitude is increased and approaches the stochastic threshold. These structures can be related to the form of the corresponding velocity space distributions, which show trapping in the wave potential. Conversely, from a knowledge of linearly and non-linearly perturbed particle orbits, one can obtain information about the self-consistent plasma wave fields that have generated such orbits, independently of any a priori assumptions on the linearity of the plasma response.

### **Conclusions**

The onset of chaos has been studied within different diagnostic approaches, providing a plasma description ranging from the collective properties to the test-particle orbit characteristics. The velocity space transport has been observed to increase abruptly for large regions of the particle phase space when the stochastic threshold for the wave excitation amplitude is reached. Saturation of the heating and transport process is observed both in the macroscopic and test-particle plasma representations and seems to indicate that wave-particle chaos is self-limited.

*This work was partly supported by the Fonds National pour la Recherche Scientifique. The authors would like to thank Dr.M.Q.Tran for helpful discussions and P.J.Paris for help with the experiments.*

<sup>†</sup>Permanent address: Lab. for Plasma Research, Univ. of Maryland at College Park, MD 20742, USA.

### **References**

- <sup>1</sup>D.R.Shklyar, *Planet. Space Sci.* **34**, 1091 (1986).
- <sup>2</sup>G.M.Zaslavsky and N.N.Filonenko, *Sov. Phys. JETP* **25**, 851 (1968).
- <sup>3</sup>W.Kerner et al., *this conference*.
- <sup>4</sup>L.C.Appel et al., *this conference*.
- <sup>5</sup>A.Fasoli et al., *Phys. Rev. Lett.* **70**, 303 (1993).
- <sup>6</sup>F.Skiff et al., *Phys. Lett. A* **137**, 57 (1989).
- <sup>7</sup>D.F.Escande, *Phys. Report* **121**, 166 (1985).
- <sup>8</sup>M.Fivaz et al., *Phys. Lett. A* **182**, 426 (1993).
- <sup>9</sup>A.Fasoli et al., *Phys. Rev. Lett.* **68**, 2925 (1992).
- <sup>10</sup>R.Z.Sagdeev, D.A.Usikov and G.M.Zaslavsky, *Non-linear Physics* (Harwood Academic, Chur, 1988)

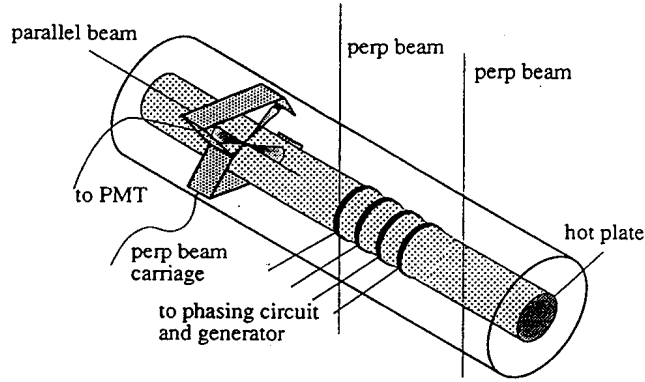


**Fig.1** LMP experimental arrangement

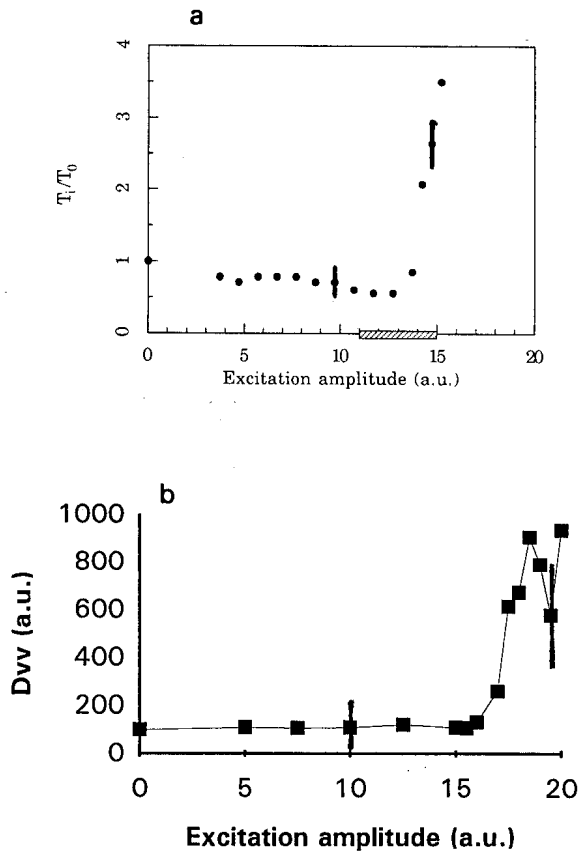


**Fig.2** Parallel temperature (a) and  $v$ -space diffusion coefficient (averaged over the wave phases) (b) vs. excitation amplitude.  $D_{wv}$  is measured from the spread in the time of flight spectra of tagged particles. Here and in Fig.3, the excitation frequency is  $f=25$  kHz. The shaded area corresponds to  $K=1$ .

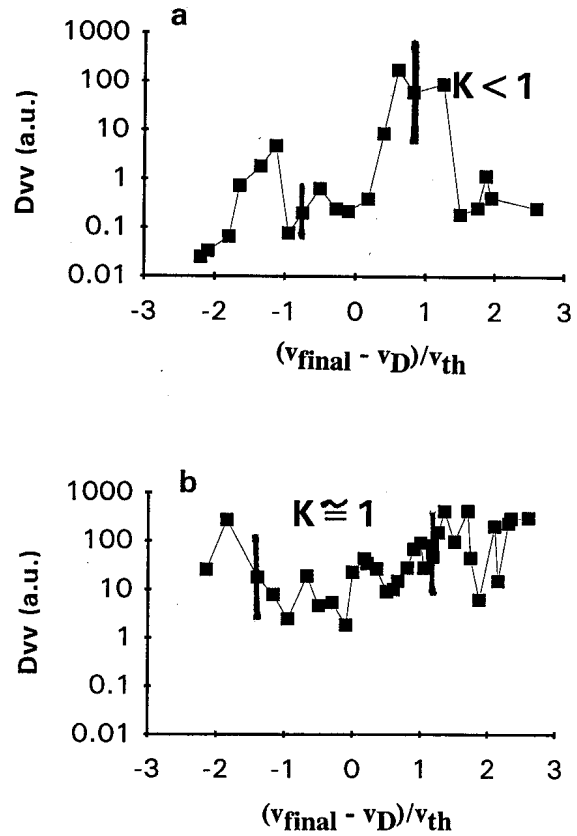


**Fig.3** Local  $D_{wv}$  as a function of the velocity for two different wave amplitudes: (a)  $K < 1$ ; (b)  $K \approx 1$ . Here the wave excitation is pulsed so that the wave phase is synchronous with the tag beam and the tagged particles see always the same phase at the same location.

## MEASUREMENT OF THE OPTICAL DEPTH AT THE THIRD ELECTRON CYCLOTRON HARMONIC IN TORE SUPRA

J.L. Ségui, Y. Michelot, G. Giruzzi

*Association EURATOM-CEA sur la Fusion  
Département de Recherches sur la Fusion Contrôlée  
Centre d'Etudes de Cadarache  
13108 St. Paul-lez-Durance (FRANCE)*

T. Goodman, A. Kritza<sup>a</sup>, A. Pochelon, O. Sauter, G.R. Smith<sup>b</sup>, M.Q. Tran

*Association EURATOM-Confédération Suisse  
Ecole Polytechnique Fédérale de Lausanne  
Centre de Recherche en Physique des Plasmas  
1007 Lausanne (SWITZERLAND)*

Electron cyclotron absorption of extraordinary waves at the third harmonic has important applications for heating in toroidal plasmas, in particular for devices working at low magnetic field and in high density regimes. Such machines include stellarators, reversed-field pinches and tokamaks devoted to high-beta plasma studies; for example, TCV (Tokamak à Configurations Variables [1]) with plasma elongations up to  $b/a = 3$ . The main drawback of 3rd harmonic ECRH is related to the relatively low optical depth predicted by the linear relativistic theory [2], which sets constraints both on the launching geometry and on the minimum electron temperature for which the method is applicable. Since the value of the first-pass absorption is a critical issue of this heating scheme, it is important to verify the theoretical evaluations of the optical depth of a Maxwellian plasma with experiments. This motivated the experimental transmission measurements performed on Tore Supra, using a vertically propagating extraordinary mode at variable frequency. In contrast with horizontal propagation, the use of vertical propagation allows a detailed comparison with the relativistic theory of wave absorption and ray propagation. In fact, along a vertical chord the toroidal magnetic field is nearly constant and the cyclotron frequency is slowly varying, basically because of the poloidal field and of paramagnetic and diamagnetic effects. This means that the shape of the optical depth as a function of frequency is very close to that of the local absorption coefficient and a precise measurement of the optical depth will be a sensitive check of the absorption theory including, e.g., relativistic ray-tracing and gyrokinetic corrections [3]. In the past, optical depth measurements have been performed in stellarators [4,5] and in tokamaks in the horizontal direction [6-8]. Vertical transmission measurements have been performed basically as a diagnostic of superthermal electrons [9-11] and of MHD modes [12].

The experimental arrangement used is the following. A narrow beam of microwaves (spread angle  $< 2^\circ$ ) is launched into the torus from a bottom port along a vertical direction intersecting the magnetic axis of a standard discharge. Both launching and receiving antennae

---

<sup>a</sup> Lehigh University, Bethlehem, Pennsylvania (USA)

<sup>b</sup> LLNL, Livermore, California (USA)

are rectangular horns, with the longest side parallel to the direction of the magnetic field at the plasma/vacuum interface, in order to couple a pure extraordinary mode and to minimize Faraday and Cotton-Mouton effects. A millimeter wave source of the IMPATT type is used (power  $\geq 5$  mW; frequency range 99-109 GHz).

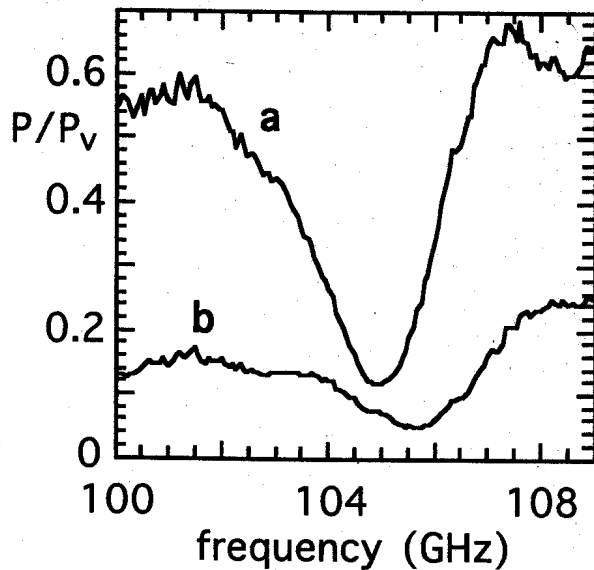


Fig. 1: Transmission spectra. a) low density; b) high density

In order to enhance the signal-to-noise ratio, the launched beam is amplitude-modulated at the frequency  $f_0 = 200$  kHz, and the received signal is video-detected through a low-pass filter (20 kHz band). The result is an average signal-to-noise ratio higher than 20 dB. The problem of standing wave formation due to multiple wall reflections is avoided, to a large extent, because of the natural divergence of the beam used and by the presence of large oblique port windows. The time resolution is determined by the frequency sweeping time of the wave source ( $\approx 3$  ms). The experiments have been performed in the Tore Supra tokamak ( $a = 0.78$  m,  $R = 2.36$  m) in Ohmic discharges at a toroidal magnetic field  $B \approx 1.25$  Tesla. The main parameters scanned are the density ( $10^{19} < n_{e0} < 3 \times 10^{19} \text{ m}^{-3}$ ) and the plasma current ( $150 < I_p < 600$  kA), which results in temperature variations in the range  $0.8 < T_{e0} < 1.2$  keV. The density profiles are measured by a 5-chord infrared interferometer and the temperature profile by a 12-channel Thomson scattering system.

Typical examples of measured spectra are shown in Fig. 1, for central densities of  $1.4 \times 10^{19} \text{ m}^{-3}$  (a) and  $2.8 \times 10^{19} \text{ m}^{-3}$  (b). The quantity plotted versus frequency is the power detected by the receiving antenna normalized to the corresponding power measured in vacuum ( $P/P_v$ ).  $P$  is reduced with respect to  $P_v$  because of two effects: refraction losses (namely broadening and deflection of the wave beam) which decrease with increasing frequency, and wave absorption, which is localized close to the 3rd harmonic of the cyclotron frequency  $\omega_c$ . The level of the signal far from  $3\omega_c$  (i.e., where the absorption vanishes) gives a measurement of refraction losses, which are generally found to decrease linearly with frequency in the narrow frequency range considered (10 GHz). This allows the separation of refraction effects from absorption and the precise measurement of the optical depth  $\tau_{X3}$ . Refraction losses grow with the

$n_e$  and  $P/P_v$  decreases with increasing  $n_e$ . The dip in the transmission spectra is deeper and broader at higher densities.

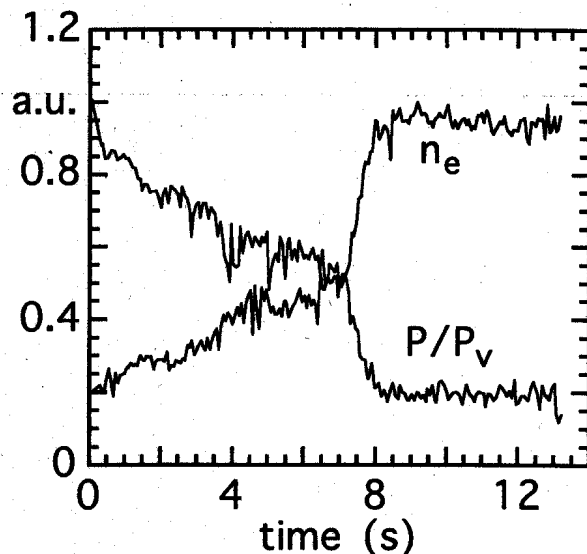


Fig. 2: Time behaviour of electron density and transmission signal at fixed frequency



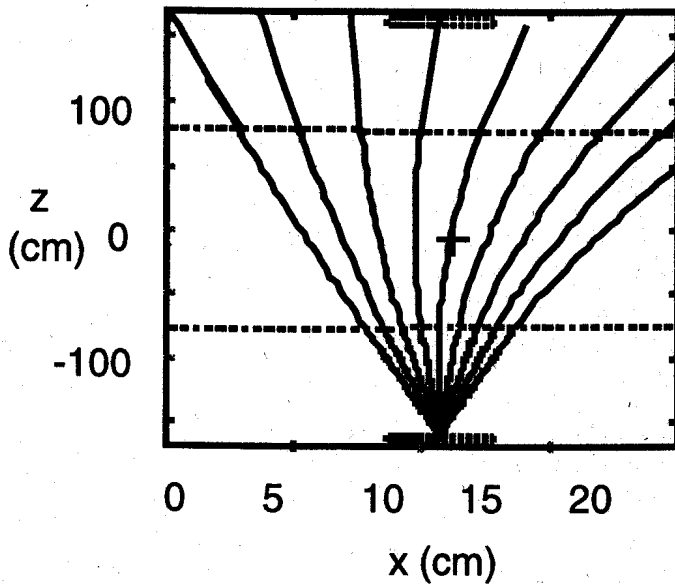


Fig. 3 : Poloidal projection of the ray trajectories between the two antennae. A + indicates the position of the magnetic axis

current the spectra present a bump close to  $\omega_c$ , on the high frequency side of the dip in transmission. This effect is systematically observed and appears related to hot plasma effects on the ray propagation. The measured transmission coefficient  $\exp(-\tau_{X3})$  is now compared to the theoretical values, obtained by integrating along the ray trajectories the local absorption coefficient [2]

$$\alpha_{X3} \approx \frac{\omega}{cN_x} \left(1 - \frac{i\epsilon_{12}}{\epsilon_{11}}\right)^2 \left(\frac{N_x}{Y}\right)^4 \frac{9}{7!} \left(\frac{\omega_p}{\omega}\right)^2 \frac{\sqrt{2\pi}}{\mu} (2Z)^{7/2} \exp(-Z), \quad (1)$$

where  $N_x$  is the cold plasma refractive index,  $\epsilon_{12}$ ,  $\epsilon_{11}$  are elements of the cold dielectric tensor,  $\mu = mc^2/T_e$ ,  $Y = \omega_c/\omega$  and  $Z = \mu(3Y - 1)$ . The finite size of the antennae is taken into account by averaging over multiple rays. A typical experimental spectrum is shown in Fig. 5 (dashed line), together with two theoretical curves (solid lines) which cover the error bars in the measured density and temperature profiles. The agreement is good, although the experimental curve looks somewhat broader; this is probably due to lack of precision in the evaluation of the magnetic equilibrium. Equation (1) shows that  $\alpha_{X3}$  is maximum at  $Z = 7/2$  and that the maximum optical depth for vertical propagation will be proportional to the line-averaged values of  $n_e T_e$ , at least at moderate densities. This dependence has been checked by slowly increasing the density during a

density, as shown in Fig. 1, as well as in Fig. 2, where the time evolution of both  $P/P_v$  and the line-averaged density is shown for a case in which the density was increased by gas puffing during the discharge. Refraction effects have limited the experimental range to moderate densities. Typical ray trajectories obtained in this density range by ray-tracing calculations are shown in Fig. 3. An important effect to be included in ray-tracing and absorption calculations is the paramagnetic correction to the toroidal field ( $\approx 3\%$  of the vacuum field) due to the plasma current. This effect causes a measurable frequency shift of the absorption line as the current is varied, as shown in Fig. 4. Note that at low

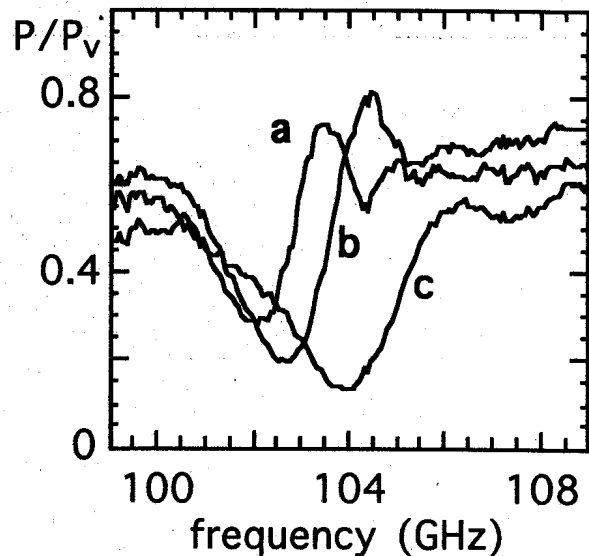


Fig. 4: Transmission spectra. a)  $I_p = 180$  kA; b)  $I_p = 300$  kA; c)  $I_p = 550$  kA

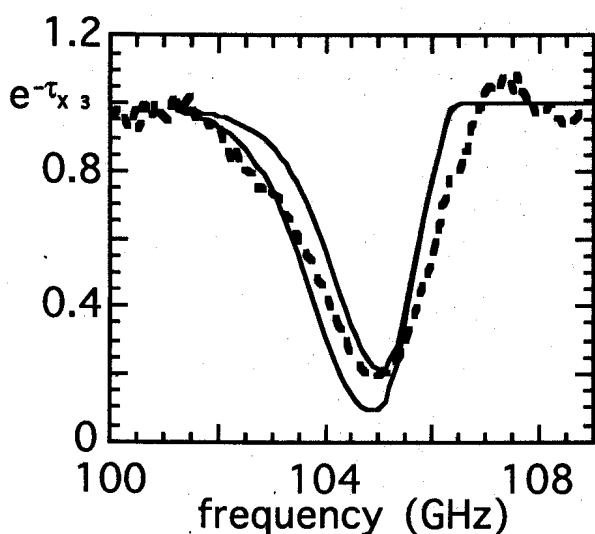


Fig. 5 : Experimental (dashed) and theoretical (solid lines) transmission coefficients

line being rather narrow and sensitive to paramagnetic effects, this heating scenario calls for a sophisticated launching system, providing good localization, low beam divergence and good control of the launching angles.

**Acknowledgements.** This work has been partly supported by the Swiss National Science Foundation.

- [1] G. Tonetti et al., in *Proc. of 16th. Symp. on Fusion Technology, London 1990*, 1, 587.
- [2] M. Bornatici et al., *Nucl. Fusion* 23, 1153 (1983).
- [3] D.C. McDonald et al., *Phys. Plasmas* 1, 842 (1994).
- [4] E.B. Meservey, S.P. Schlesinger, *Phys. Fluids* 8, 500 (1965).
- [5] V. Arunasalam et al., *Phys. Fluids* 11, 1076 (1968).
- [6] P.C. Efthimion et al., *Phys. Rev. Lett.* 44, 396 (1980).
- [7] A. Pachtman et al., *Nucl. Fusion* 27, 1283 (1987).
- [8] F. Smits et al., in *Proc. 8th Joint Workshop on ECE and ECRH, Gut Ising 1992*, (IPP, Garching, 1993) 2, 513.
- [9] E. Mazzucato et al., *Nucl. Fusion* 25, 1681 (1985).
- [10] R. Kirkwood et al., *Nucl. Fusion* 30, 431 (1990).
- [11] J.L. Ségui, G. Giruzzi, *Plasma Phys. Contr. Fusion* 36, 897 (1994).
- [12] G. Giruzzi et al., *Nucl. Fusion* 31, 2158 (1991).
- [13] R.L. Meyer, I. Fidone, in *Proc. 6th Joint Workshop on ECE and ECRH, Oxford 1987* (Culham, 1987), 57.
- [14] A. Pochelon et al., in *Proc. 20th JEPS Conf. Contr. Fusion Plasma Phys., Lisbon 1993* (EPS, Geneva, 1993), 17C, III, 1029.

current flat-top: the temperature also changes, which gives an excursion in the parameter  $n_e T_e$ . The measured values of the maximum optical depth  $\tau_{\max}$  are plotted versus  $n_{e0} T_{e0}$  in Fig. 6. Within the error bars, a reasonable agreement is found with the theoretical prediction.

In conclusion, direct experimental measurements of the optical depth have given a global confirmation of the relativistic theory of wave absorption at the 3rd electron cyclotron harmonic. These results are a sound basis for heating experiments at the 3rd harmonic. For adequate first-pass absorption, long path lengths are required and the microwave beam needs to be launched at a shallow angle to the resonance line, i.e., nearly vertically [13,14]. However, the absorption

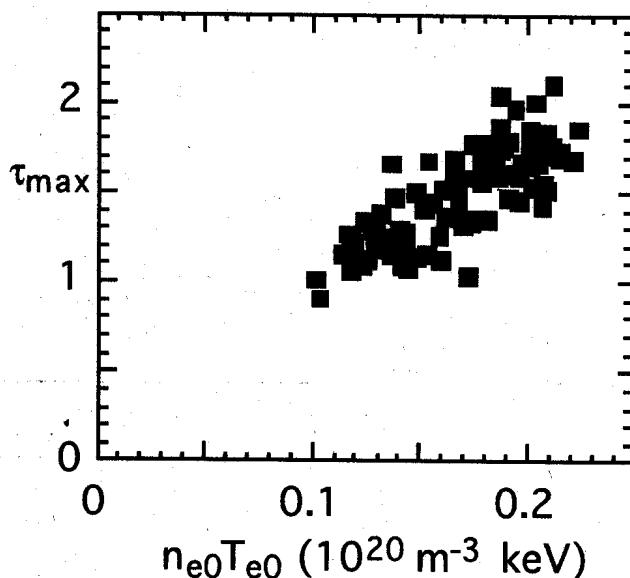


Fig. 6 : measured maximum optical depth for vertical propagation vs  $n_{e0} T_{e0}$

## The Dynamics of Shaping Control in TCV

J.B. Lister, Y. Martin, J.-M. Moret

Centre de Recherche en Physique des Plasmas  
Association EURATOM - Confédération Suisse  
École Polytechnique Fédérale de Lausanne  
CH-1007 Lausanne, Switzerland

**Abstract:** Precise control of the plasma position and shape during a discharge is important for several reasons. The vertical movement, unstable in shaped TCV plasmas, must be under optimised feedback control in order to achieve the highest performances foreseen. The radial position must be maintained to respect plasma-wall spacing. The elongation and triangularity must be closely controlled at high current to maintain the safety factor close to its limits.

These requirements are met in the steady state by precise measurement algorithms, but when the plasma shape or internal parameters are changing rapidly, the dynamic properties of the different feedback loops become crucial. In order to study these effects, perturbation injection experiments have been performed. A linear interpretation of the results requires simple models of the plasma behaviour and of the coil and vessel system. The shape of the TCV vacuum vessel is such that more than one vessel eigenmode must be retained. The control loops can have integral feedback as well as proportional and derivative terms.

**Introduction:** In order to control shaped plasmas we must perform 4 operations. Firstly, we must define a set of parameters which are to be controlled. Secondly, we must find a way of extracting these parameters from the signals available in real-time. Thirdly, we must generate the reference inputs corresponding to these control parameters as inputs to the control loop. Finally, we must feedback the errors on these parameters to the available control inputs. Complementary to these actions, we must measure the control loop, the system to be controlled, as well as establish a model which can be the basis for comparison with the experimental results. We ignore the density feedback although it is performed by the same hardware and software.

Each of these actions can be approached in many ways, and the flexibility of the TCV Plasma Control System (PCS) has already allowed many approaches to be tested, for example [1]. This paper deals briefly with all of these points, as they have been applied to some of the plasma shaping and control experiments on the TCV tokamak.

**Definition of the Control Parameters:** The TCV magnetics system generates a total of 120 signals for use in the PCS: poloidal field probes inside the vacuum vessel ( $B_{pol}$ ), differential flux-loops on the outer surface of the vessel ( $\Psi$ ) and measurements of the toroidal and poloidal field coil currents ( $I_{pol}$ ). We can imagine creating control parameters of intuitive significance, such as elongation, triangularity, major radius. A consequent problem is that the mapping between available inputs signals and these "physics" variables is non-linear, a problem successfully addressed using Function Parameterisation (ASDEX-UG) or Neural Networks (TCV, COMPASS). Solving this mapping problem leaves us with a similar problem which is that mapping the errors in this control parameter space to the corrections of the control coil currents is now also non-linear. We conceived the TCV PCS hardware for yet another approach, namely to construct a piecewise-linear mapping, switching the matrices for parameter extraction and the controller as the discharge evolves. In some ways this simple approach marries the worst aspects of both linear and non-linear parameter extraction and has not yet been used for creating TCV plasmas.

We have chosen to retain a linear extraction of the control parameters, using a single A-matrix (Fig 1.), and with a constant controller (P-,I-,D-matrices). The extraction of the plasma current and the vertical position are performed as discrete sums over the input signals, approximating the appropriate contour integrals. There remain some open questions concerning the optimisation of this approximation for extracting  $z \cdot I_p$  for avoiding phase-shift problems at high frequency. The shape control parameters have been defined heuristically, using combinations of  $[B_{pol}, \Psi, I_{pol}]$  which intuitively are dominated by certain shape characteristics, such as radial position, inner triangularity and outer triangularity. Other than this intuitive predominance we only require linear independence.

Parameter Extraction: Having defined these linear combinations of input signals, the question of extraction of these parameters in real-time is trivialised. The A-matrix (Fig. 1) is defined by the combinations themselves, and remained constant in time during a single shot, and constant from shot to shot for discharges up to elongation of 1.74 and both positive and negative triangularity.

Reference Waveform Creation: The waveforms of the control parameter references,  $CP(t)$ , are non-linearly related to the “physics” waveforms,  $Phys(t)$ , such as triangularity and kappa. Initially, these references were drawn intuitively by hand, but subsequently we have automated this using a Neural Network Multi-Layer Perceptron trained over a series of discharges which were obtained “manually”. At present the “pilot” can draw the  $Phys(t)$  and request the MLP to derive the  $CP(t)$  during the shot preparation.

Pre-Programming Waveform Creation: The TCV power amplifiers have the option of a current feedforward control input in addition to the normal voltage control signal, and we mix the feedback control voltages with voltage feedforward signals. Choosing the  $CP(t)$  to be linearly related to the inputs signals gives us the significant advantage that the mapping  $CP(t) \rightarrow I_{pol}(t)$  is almost linear, and good enough for use in feedforward. The  $I_{pol}(t)$  are therefore generated by a linear mapping derived by SVD of the dependencies found in achieved discharges. This approach also allows us to run multiple shaping coils with an under-constrained feedback control. In other words, we can now preprogram the 16 shaping supplies and use only a few  $CP(t)$  to correct the particular shape parameters chosen. The preprogramming of the ohmic transformer current is obtained by subtracting the volt-second contributions of the shaping supplies, and assuming a simplified evolution of the resistive voltage over 4 phases of the discharge. We derive the voltage feedforward waveforms from  $U_{pol}(t) = M \cdot dI_{pol}(t)/dt$ , where the M-matrix is defined with no vessel and no plasma. The errors inherent in these simplified preprogramming algorithms are all recovered in the feedback loop. The presence of the feedforward signals allows us to reduce the gain in the feedback, as well as work underconstrained, as mentioned.

Controller Design: The TCV PCS allows all controllers of the form:

$$\overrightarrow{\delta \dot{I}_{pol}} = \left[ \mathbf{P} \cdot \text{diag}\left(\frac{1}{\tau_P}\right) + \mathbf{D} \cdot \text{diag}\left(s \cdot \frac{\tau_D}{\tau_P}\right) + \mathbf{I} \cdot \text{diag}\left(\frac{1}{s \cdot \tau_I \cdot \tau_D}\right) \right] \cdot \overrightarrow{\epsilon_{CP}}$$

Current feedback is performed assuming a typical plasma inductance, and correcting the mid-plane total flux. The  $z \cdot I_p$  feedback is more delicate, and is performed by a specifiable ratio of the control coil currents, normalised for their  $B_r$  contributions on axis. The chosen combinations can be different for the P-, I-, D-sub-matrices. The shape  $CP(t)$  feedback is performed using identical P-, I-, D-sub-matrices and the same  $(\tau_P, \tau_I)$  using the approximation :

$$\overrightarrow{\delta I_{pol}} = \left( \mathbf{A} \cdot \frac{\partial [B, \Psi, I_{pol}]}{\partial I_{pol}} \right)^{-1} \cdot \overrightarrow{\epsilon_{CP}}$$

where the sensitivities are measured with no plasma and no vessel. This approximation has been found to be adequate and robust. A useful validation of the heuristic choice of the CP is the conditioning of the matrix inverted in the above equation. The values of  $\tau_p, \tau_D, \tau_I$  are chosen to produce the desired closed-loop responses.

**Modelling:** We have had to extend the simple DIII-D model of vertical motion [2] for TCV for 2 reasons. The irregular shape of the vessel and its resistance contour force us to keep more eigenmodes of the vessel current distribution. They are not only important spatially, but their eigenvalues do not decrease as fast as in the more conformal DIII-D vessel. Placing the plasma at different z-positions has also forced us to use more eigenmodes. The full model of the vertical motion becomes :

$$\begin{bmatrix} s \cdot M_e + R_e & s \cdot \frac{\partial M_{ep}(z)}{\partial z} \\ s \cdot \frac{\partial M_{ep}(z)}{\partial z} & s \frac{2\pi R}{I_p} \frac{\partial B_r(I_{pol})}{\partial z} \end{bmatrix} \begin{bmatrix} I_e \\ z \cdot I_p \end{bmatrix} = \begin{bmatrix} 0 \\ 0 \end{bmatrix}; \quad \alpha(z, I_{pol}) = \frac{\frac{2\pi R}{I_p} \cdot \frac{\partial B_r(I_{pol})}{\partial z}}{\sum \frac{\left(\frac{\partial M_{ep}(z)}{\partial z}\right)^2}{L_e}}$$

alpha is equal to the ratio  $n/n_c$  previously used, but this expression is more suitable for use with many eigenmodes as the numerator and denominator are calculable separately for the vessel and for the vacuum field. We also eliminate the vertical field from the expression. The poles of this extended model can then be derived as a function of the parameter alpha as well as the number of eigenmodes considered. There is always one and only one unstable pole, dependent on alpha, and on the number of eigenmodes, Fig. 2. The remaining stable poles vary as more eigenmodes are added, but are almost insensitive to changes in alpha.

Experiments using a cut in the vertical control were compared with a full model in the code NOVA-W. This expanded eigenmode model predicts a growth rate of  $496 \text{ s}^{-1}$ , within 20 % of both the full calculation and the experiment. The expanded model also suggests that we have succeeded in stabilising plasmas with unstable growth rates over  $800 \text{ s}^{-1}$ , using the algorithms described here, and in [1].

**Measurements of the Closed Loop:** In a series of exploratory experiments, we have injected perturbations into the proportional controller for the  $z \cdot I_p$  error. This perturbation allows us to determine the poles of the closed loop system as the system evolves during shaping. These experiments are also being used to study the properties of the different coil pairs which can be used for vertical position control. The response gives a picture of the closed loop which has enabled us to optimise the controller time-constants, Fig. 3. However it also includes the dynamics of the power amplifiers.

**Measurements of the System:** Experiments were also performed by injecting square pulses into the coil demand voltages, for 8 up-down symmetric pairs of coils, during a single pulse with constant parameters and weak elongation, giving weak unstable growth rates. The feedback loop adjusts the voltages applied to all shaping coils to maintain the control parameters at their references, thereby “weakening” the perturbation. The actual voltages applied to all coils were used as multiple time-varying inputs to a single system (coils, vessel, plasmas). This method [3] allows us to explore the poles and zeros of the system, with no “discrepancies” between separate experiments with particular coils excited. This approach should ultimately lead to the design of an optimised controller.

**Conclusion:** We have operated a shaping algorithm using linear control parameters which are fixed over a wide range of plasma currents and shapes. The algorithm for deriving the

references, deriving the controller and deriving the feedforward waveforms has proven to be flexible and robust. Growth rates over  $800 \text{ s}^{-1}$  have been stabilised using a simple  $z \cdot I_p$  observer and controller which may need more study, or may be taking our plasmas to the growth rate limits imposed by the switching rate of the power supplies. This optimisation of the controller time-constants was performed using the closed-loop response to injected perturbations.

It is a pleasure to acknowledge the support of the full TCV team. This work was partly supported by the Fonds National Suisse de la Recherche Scientifique.

References:

- [1] F. Hofmann, this conference
- [2] E.A. Lazarus, J.B. Lister, G.H. Nielson, Nucl. Fus. 30 (1990) 111
- [3] J.M. Moret, EUR-CEA-FC-1409 (1990)

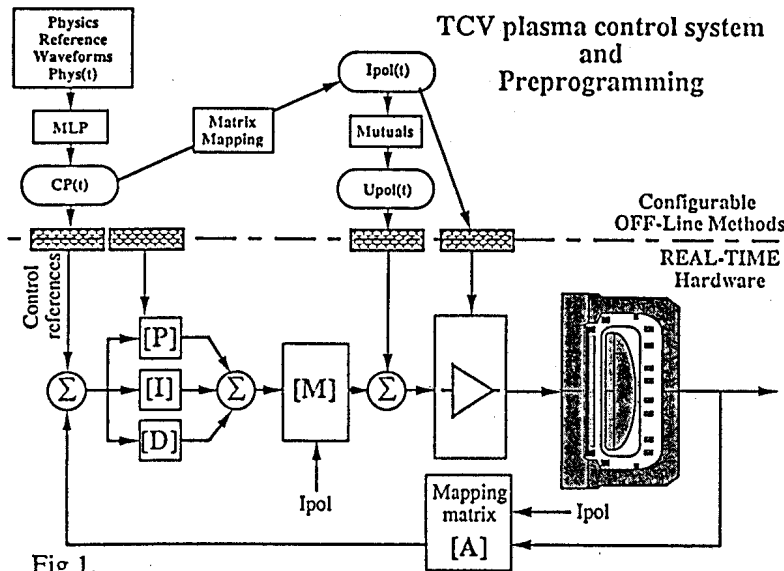


Fig 1.

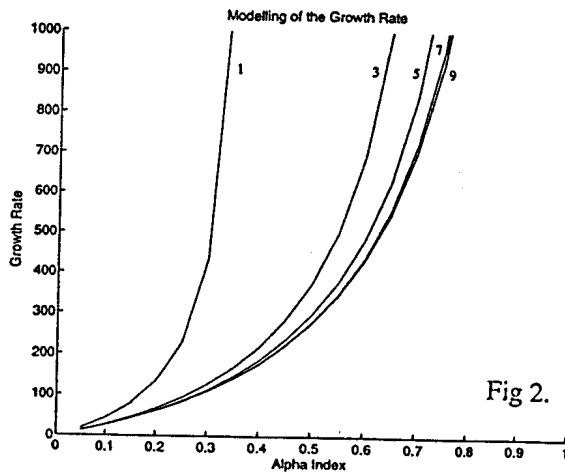


Fig 2.

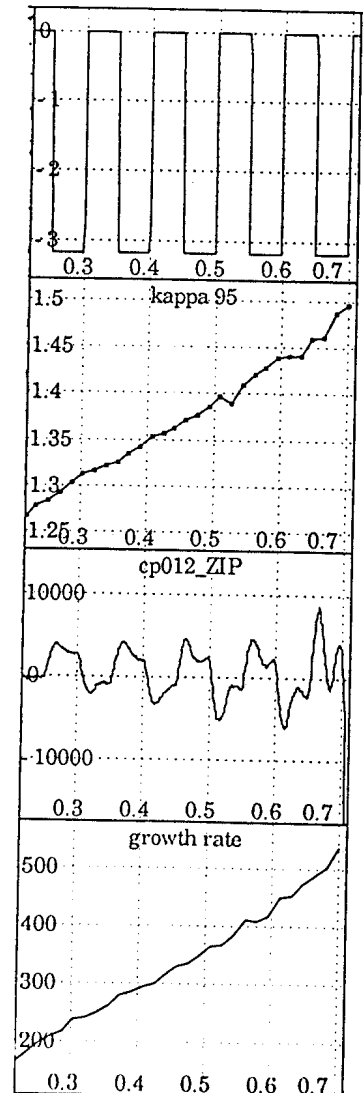


Fig 3.

Fig 1: PCS layout.

Fig 2: Calculated growth rate, varying the number of modes.

Fig 3:  $z \cdot I_p$  perturbation injection in a shaping ramp.

## **Studies of the density limit of elongated plasmas in TCV using a FIR interferometer**

C.Nieswand, R.Behn, F.Buhlmann, F.Hofmann, Y.Martin

Centre de Recherches en Physique de Plasmas

Association Euratom - Confédération Suisse

Ecole Polytechnique Fédérale de Lausanne

### **Introduction**

The main plasma density diagnostic on the tokamak TCV is a multichannel FIR interferometer. The system is operated during each shot and provides the signal for the density feedback of TCV. First measurements with the system are presented: observation of mode-locking, determination of the Hugill plot and observation of profile changes during H-mode.

### **The interferometer system**

The FIR laser is optically pumped by a cw CO<sub>2</sub> laser and is operated at the 214.6 $\mu$ m line of CH<sub>2</sub>F<sub>2</sub>. The laser power is about 70mW and is actively stabilized by tuning the pump frequency and the cavity length of the FIR laser.

The wavelength allows for operating the system over a wide range of plasma densities ( $5 \cdot 10^{17} \text{m}^{-3}$  -  $5 \cdot 10^{20} \text{m}^{-3}$ ) and plasma configurations with only minor refraction of the probing laser beam. The Faraday rotation angle for typical TCV plasmas is sufficiently large for a future upgrade of the system to a polarimeter.

The laser is placed in a separate room about 8m away from TCV. The beam is transferred to the interferometer by 25mm diam. pyrex oversized waveguides.

Absorption of the beam in humid air is significant. Therefore boxes made of a rigid honeycomb fibreglass material contain all optical elements. The boxes and the waveguides are flushed either with dry nitrogen or dried air.

The boxes are mounted on a stable concrete/fibreglass support structure close to TCV which is completely decoupled from the tokamak structure in order to minimize the transmission of vibrations from the tokamak to the interferometer system. Compensation of residual perturbations will be achieved by an interferometer at 830nm which will be added to the system.

The interferometer is of Mach-Zehnder type and is similar to the systems on TEXT (upgrade) [1], MTX [2] and RTP [3]. The probe beam which is broadened to a slablike beam traverses the plasma from the bottom to the top (see figure 1). Large windows on the top and bottom of the machine allow for almost complete illumination of the plasma cross section. The reference beam is frequency shifted by a rotating grating and is broadened up to the same size as the probe beam. Both beams are superposed on a crystal quartz beamcombiner.

Presently a set of only 4 pyroelectric detectors is mounted on the system. The collection optics of each detector determines the radial position and the spatial resolution (approx. 20mm) of the corresponding chord (see figure 1). The detectors and the mixer electronics presently limit the bandwidth of the system to 6kHz. The laser power per channel is about 0.5mW which is close to the limit for the existing pyroelectric detectors. They will be replaced by a set of 15 more sensitive and faster InSb detectors which allow for an upgrade to a polarimeter system.

The signal of the central beam is fed to a fringe counter which provides a real time signal proportional to the line integrated density and which is used for feedback control of the density in TCV. Furthermore, the FIR interferometer is used in the absolute density calibration of the Thomson scattering diagnostic [4].

## Measurements

In the initial implementation only the central interferometer channel was operational. The excellent signal to noise ratio enabled the observation of mode-locking, which occurred in some shots. Figure 2 shows plasma current, density and soft X ray traces. It shows the growing amplitude ( up to 4% density modulation) and the increasing period until the mode completely locks which leads to a minor or major disruption several milliseconds later.

A systematic investigation of density limits is not yet complete since the number of shots with density measurements is still limited and the operational regime of TCV is not yet fully exploited.

Figure 3a shows the Hugill diagram with data from 400 shots (disrupted, non-disrupted, D-shaped, X-point, a variety of elongations and ohmic power, different wall conditions etc.). The highest value of  $\langle n_e \rangle R_{q95}/B$  of about 30 was obtained in diverted H-modes after the first boronisation of TCV. Figure 3b shows a number of H-mode discharges before and after boronisation. The operational regime was clearly limited to  $\langle n_e \rangle R_{q95}/B < 10$  before boronisation and was substantially extended to higher Murakami parameters after boronisation. In these H-mode discharges the gas valve was completely closed by the density feedback so that the density was solely determined by recycling and was uncontrollable.

These discharges lead to a density limit disruption only in case of ELM-free H-modes or H-modes with very low ELM activity in which the density rises continuously until the disruption occurs. However in strongly ELMing H-mode phases the plasma makes the transition to L-mode before it disrupts as previously reported on Asdex [5] and DIII-D [6].

In ELM free or grassy ELM H-modes the density ramp is accompanied by a permanent rise in  $q$  at the magnetic axis, a reduction of sawtooth activity and by density profile flattening. Figure 4a shows such a discharge. Starting with a short ELM phase (310-345ms), the plasma changes to an ELM-free H-mode (345-400ms), followed by a phase with grassy ELMs. At 420 ms large regular ELMs appear and stabilize the density before the plasma goes back to a grassy ELM behaviour (520ms) until the final disruption occurs (780 ms). The density profile flattens in the beginning of the ELM-free phase (the peaking parameter as defined here approaches 1 for flat profiles and is smaller for peaked profiles) compared to L-Mode, peaks again during the phase with large ELMs and flattens when the large ELMs disappear. In the late phase with reduced sawteeth activity the profile peaks again until the disruption occurs. A more detailed analysis of the large ELM phase is shown in figure 4b. An ELM is accompanied by a fast decrease of the density in the outer interferometer channels and a slower and weaker decrease in the central channels resulting in a fast peaking of the profile. Sawteeth recover the flat profile step by step until the next ELM peaks it again.

## Acknowledgements

This work was partially supported by the Swiss National Science Foundation.

## References

- [1] G.A.Hallock et al.; Rev.Sci.Instrum. **61**, 2893 (1990)
- [2] B.W.Rice; Rev.Sci.Instrum. **63**, 5002 (1992)
- [3] A.C.A.P.van Lammeren; Rev.Sci.Instrum. **61**, 2882 (1990)
- [4] R.Behn et al.; Poster A 115 this conference
- [5] A.Stäbler et al.; Nuclear Fusion **32**, 1557 (1992)
- [6] T.W.Petrie et al.; Nuclear Fusion **33**, 929 (1993)



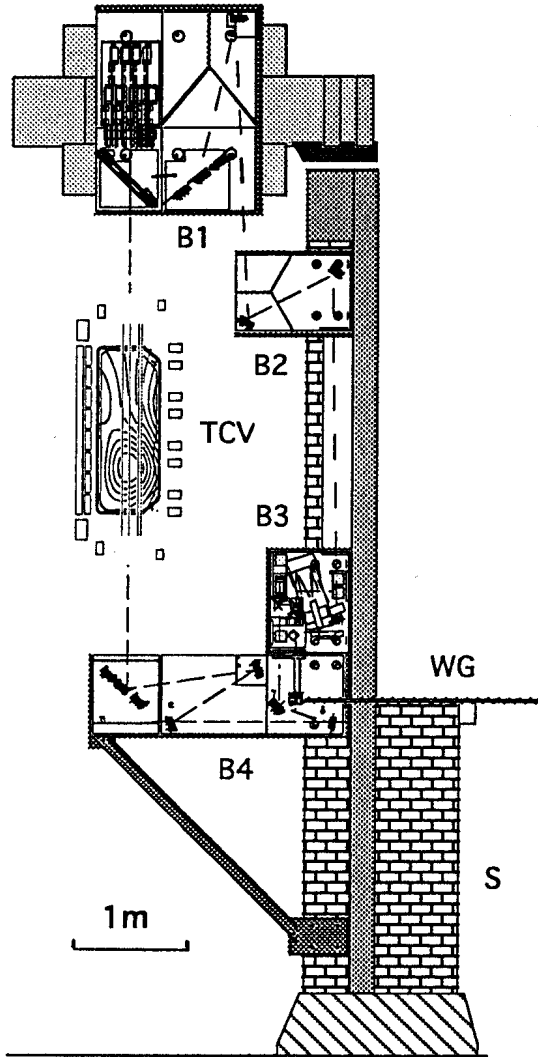


Figure 1: Interferometer TCV, S: Support structure, B1..4: Fibreglass boxes, WG: Waveguide

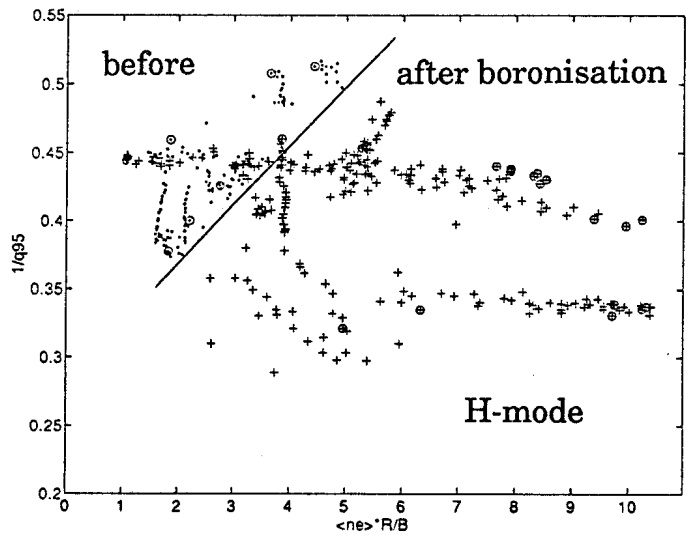
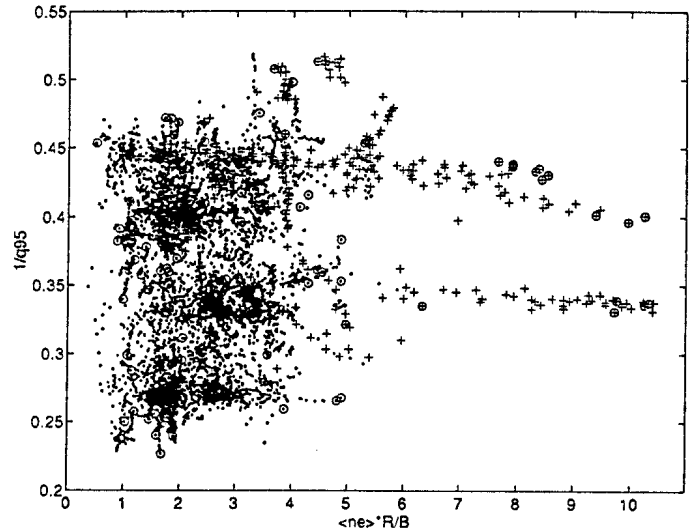


Figure 3: Hugill diagram for TCV,

a) 400 shots of any type

(. = L-mode, + = H-mode)

b) only H-mode shots

(. = before, + = after boronisation)

o denotes points just before a shot disrupted.

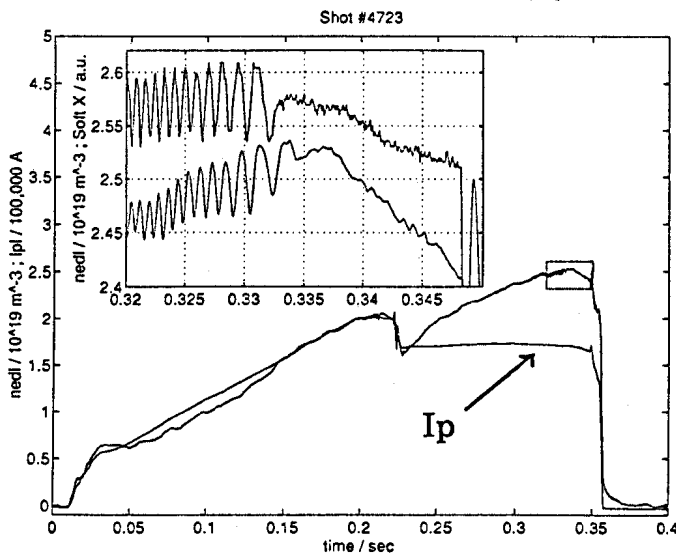


Figure 2: Locked mode : Density trace compared with central Soft X signal from two vertical chords in different toroidal sectors separated by 22.5 degrees.

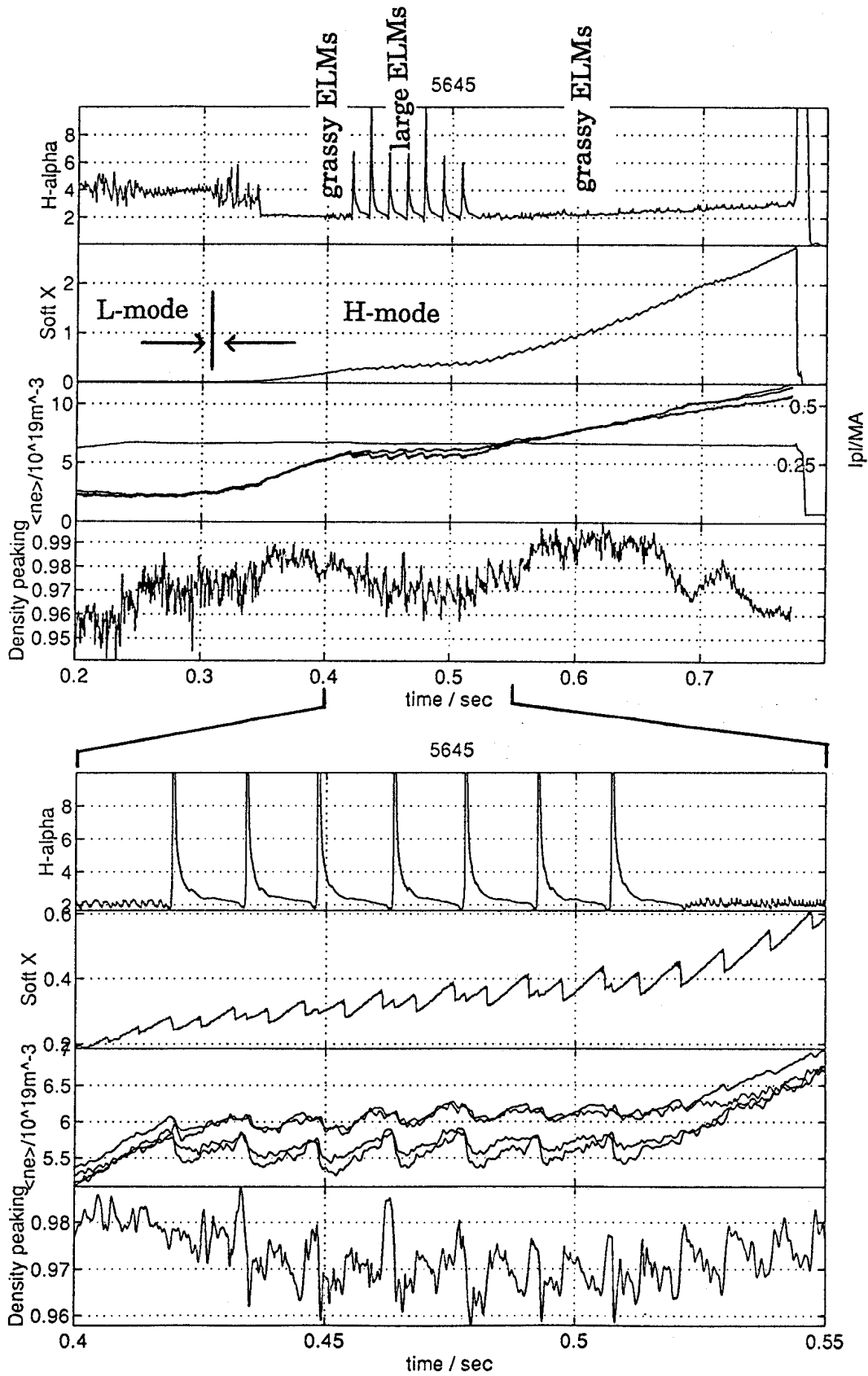


Figure 4: diverted ohmic H-mode in TCV  
a) development of the discharge b) details during a phase with large ELMs

# Ideal MHD Stability in Tokamaks with External Helical Windings

R. Moeckli, W. A. Cooper and F. Troyon  
 Centre de Recherches en Physique des Plasmas,  
 Association Euratom-Confédération Suisse,  
 Ecole Polytechnique Fédérale de Lausanne,  
 Lausanne, Switzerland

The ideal MHD stability properties of a tokamak with external  $L=3$  windings are investigated with respect to local ballooning and Mercier modes and global external modes. The energy and particle confinement in standard tokamaks is known to improve with plasma current. Imposing external helical windings offers an additional knob to vary the toroidal plasma current independently of the value of the edge rotational transform. Therefore, we can reduce the plasma current and sustain a large fraction of the rotational transform with the helical windings or conversely increase the plasma current and correspondingly unwind the rotational transform with the current in the helical coils. The aim of this study is to try to investigate the effect of the winding on local and global ideal MHD stability.

We model the effect of  $L = 3$  windings by prescribing the plasma-volume interface as

$$\begin{aligned} R &= R_{00}(1) + R_{10}(1) \cos u + \delta \cos(2u - Nv) + \delta \cos(2u - 3Nv) \\ Z &= R_{10}(1) \sin u + \delta \sin(2u - Nv) - \delta \sin(2u - 3Nv) \end{aligned}$$

where  $R_{00}(1)$  is the major axis,  $R_{10}(1)$  is the minor axis, so that  $A = R_{00}/R_{10}$  is the aspect ratio,  $u$  and  $v$  are the poloidal and toroidal angle-like respectively,  $\delta$  is the shaping parameter of the helical coil currents and  $N$  is the periods number. The configurations we studied have the following parameters :  $R_{00}(1) = 10$ ,  $R_{10}(1) = 1$ ,  $A = 10$ ,  $\delta = 0.075$  and  $N = 4$ . The resulting magnetic field produces a triangular deformation of the plasma that only alters the external region of the plasma even when the bulk of the plasma (where the pressure concentrates) remains essentially a conventional tokamak.

In a previous study [1], we allowed the q-on-axis to approach 2 and investigated the impact of external helical windings on access to the second region of MHD stability. In the work we present here, we have adjusted the plasma current profile to constrain q-on-axis to be approximately unity and consequently examine the first region of MHD stability. The equilibria were performed with the VMEC code [2].

We have applied the energy principle given by

$$\delta W_p - \omega^2 \delta W_k = 0$$

where

$$\delta W_p = \frac{1}{2} \iiint d^3x [C^2 + \gamma p |\nabla \cdot \xi|^2 - D |\xi \cdot \nabla s|^2]$$

to study the MHD stability of these configurations. The coefficients  $C^2$  and  $D$  are described in Refs. [3] and [4]. Applying the ballooning mode transformation [5], we obtain

$$\frac{\partial}{\partial \theta} \left( [C_p + C_s(\theta - \theta_k) + C_q(\theta - \theta_k)^2] \frac{\partial \chi}{\partial \theta} \right) + (1 - \lambda)[d_p + d_s(\theta - \theta_k)]\chi = 0$$

The coefficients are given in Ref. [6]. The Mercier criterion can be derived from the asymptotic analysis of the ballooning mode equation [7]. A more detailed description for the global stability can be found in [6]. The TERPSICHORE code [8] has been used for all stability calculations. The pressure profiles are optimized to satisfy marginal stability to local modes uniformly across the plasma.

We have first examined a sequence of configurations in which we have kept the toroidal plasma current fixed. The pressure, iota and current profiles of the tokamak are shown in fig. 1. Adding helical windings modifies the iota profiles as in fig. 2. We obtain that the marginal  $\beta^*$  values (defined as  $\beta^* = \frac{\sqrt{\iiint d^3x p^2} \sqrt{\iiint d^3x}}{\iiint d^3x B^2 / 2\mu_0}$ ) imposed by local ballooning/Mercier modes remain about the same. However, global external modes impose  $\beta^*$  limit in the configurations with external coils helical that are lower than that of the conventional axisymmetric tokamak.

In the second sequence we have investigated, we have modified the current profiles so that each configuration has the same value of iota at the edge ( $\iota(a) = 0.45$ ). Fig. 3 and 4 show the corresponding iota and current profiles. Using optimized pressure profiles (cf. fig. 5), we obtain that  $\beta^*$  increases slightly from  $\beta_{tok}^* = 0.986\%$  (tokamak) to  $\beta_-^* = 1.06\%$  ( $\beta_-^*$  means the marginal  $\beta^*$  value for the configuration with the current in the coils in the opposite sense than the toroidal plasma current). On the other hand, helical windings that add rotational transform make the marginal  $\beta^*$  value decrease to  $\beta_+^* = 0.804\%$ .

The calculation of the  $\beta^*$  limit imposed by global modes were performed by rescaling the ballooning/Mercier optimized pressure profile for each case with fixed edge rotational transform. The  $\beta^* = 0.905\%$  achieved in the axisymmetric tokamak appears to be optimal. This limit decrease to  $\beta^* = 0.65\%$  for the case in which the coils unwind the transform. For the case in which the transforms are additive, the  $\beta^*$  limit imposed by the global modes is  $\beta^* = 0.75\%$ . The plasma shaping that results from the external helical coils reduces the vacuum magnetic well regardless of the direction of the currents in these coils. This destabilizes the global external modes.

In conclusion, for local stability, the best marginal  $\beta^*$  value is obtained for a configuration that has higher total toroidal current than the tokamak. The marginal  $\beta^*$  value decreases for a lower total toroidal current. For global stability, the axisymmetric configuration gives the best marginal beta value with  $\beta^* = 0.905\%$ . The problem of the transition and accessibility from the first stability regime with  $q_0 \simeq 1$  to the second stability regime with  $q_0 \geq 2$  still remains an open question that requires further investigation.

Acknowledgement : This work was partly supported by the Swiss National Science Foundation.

- [1] Cooper W. A. and Troyon F., *Proc. 20th EPS Conf. Lisbon, 1993*, Vol. 17C, Part IV, EPS (1993), IV-1283

- [2] Hirshman S. P. and Betancourt O., *J. Comput. Phys.* **96** (1991) 99.
- [3] Nührenberg J. and Zille R., in *Proc. of the Workshop on Theory of Fusion Plasmas*, EUR 11336 EN (1987), pp. 3-23. Editrice Compositori, Bologna.
- [4] Anderson D. V., Cooper W. A., Gruber R. and Schwenn U., *Scientific Computing on Supercomputers II*, (Editors: J. T. Devreese and P. E. Camp), Plenum Press, New York, 1990, p. 159.
- [5] Dewar R. L. and Glasser A. H., *Physics Fluids* **26** (1983) 3038.
- [6] Cooper W.A., *Plasma Physics and Controlled Fusion* **34** (1992) 1011.
- [7] Connor J. W., Hastie J. and Taylor J. B., *Proc. R. Soc. London*, **A365** (1979)
- [8] Anderson D. V., Cooper W. A., Gruber R., Merazzi S. and Schwenn U., *Int. J. Supercomp. Appl.* **4** (1990) 34.

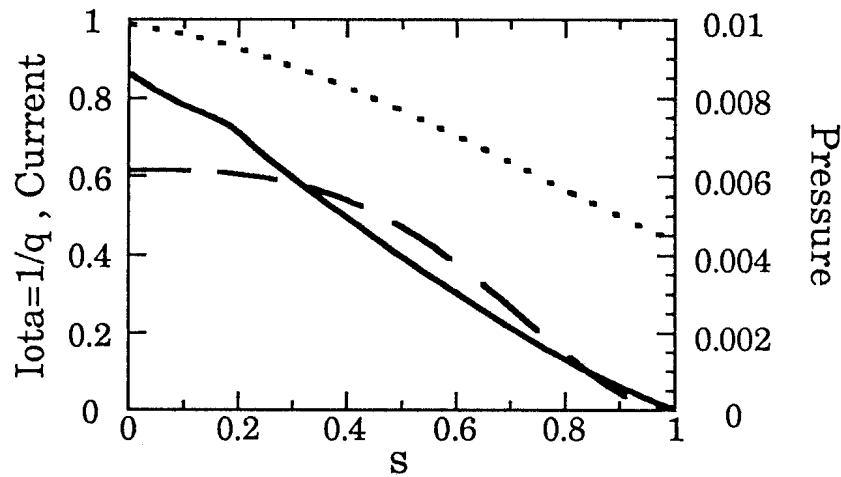


Fig. 1: Pressure (solid), iota (dotted) and current (dashed) profiles of the axisymmetric tokamak configuration.

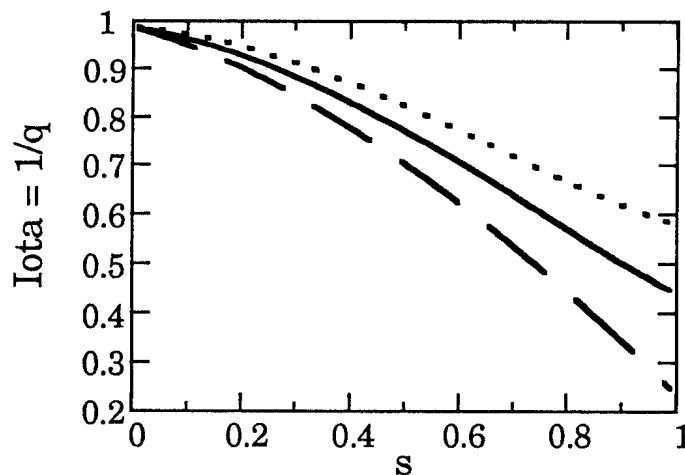


Fig. 2: Iota profiles for the sequence with constant toroidal plasma current. The solid line is the tokamak configuration. The dotted (dashed) curve corresponds to the configuration where the current in the helical coils is in the same (opposite) direction than the toroidal plasma current.

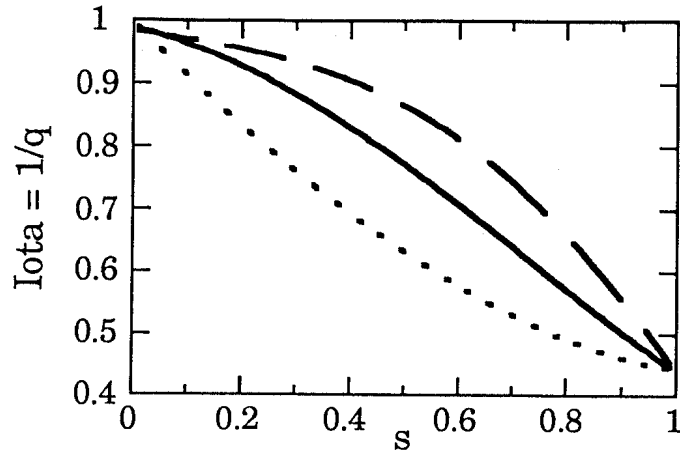


Fig. 3: The iota profiles for the sequence with constant iota value at the edge. The solid line is the tokamak configuration. The dotted (dashed) curve corresponds to the configuration where the current in the helical coils is in the same (opposite) direction than the toroidal plasma current.

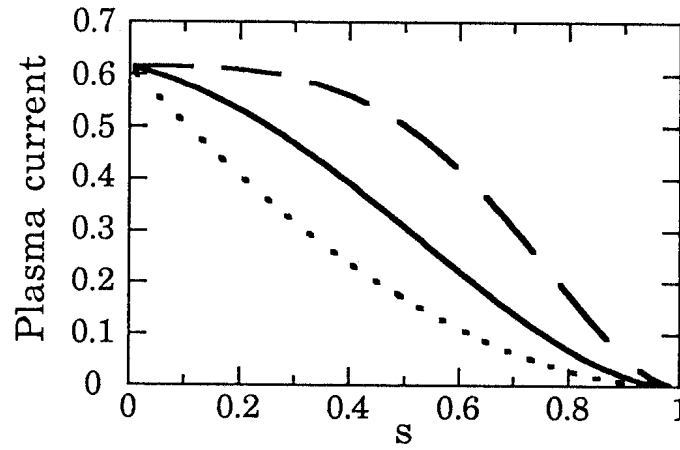


Fig. 4: The toroidal current profiles that correspond to the iota profiles of fig. 3. The solid line is the tokamak configuration. The dotted (dashed) curve corresponds to the configuration where the current in the helical coils is in the same (opposite) direction than the toroidal plasma current.

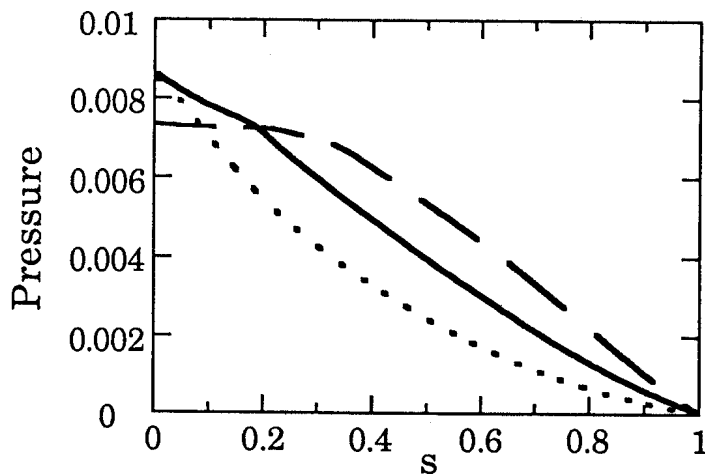


Fig. 5: The optimized pressure profiles for each configuration of the sequence with constant iota value at the edge. The solid line is the tokamak configuration. The dotted (dashed) curve corresponds to the configuration where the current in the helical coils is in the same (opposite) direction than the toroidal plasma current.

# MHD LIMITS AND AXISYMMETRIC STABILITY OF DOUBLETS

L.Degtyarev, A.Martynov, S.Medvedev

Keldysh Institute of Applied Mathematics  
Russian Academy of Sciences, Moscow

F.Troyon, L.Villard

Centre de Recherches en Physique des Plasmas  
Association Euratom - Confédération Suisse  
Ecole Polytechnique Fédérale de Lausanne

## Abstract

MHD stability limits were studied for doublet plasma configurations using the equilibrium code CAXE and the stability code KINX [1]. Beta limits have been found against ballooning and  $n=1$  external kink mode stability. For doublet plasmas in the TCV tokamak the beta limits are close to the values obtained for a plasma with a single magnetic axis and the same overall elongation. The current limit against kink modes is lower in doublets. But the maximal beta is obtained at almost the same value of the current.

Axisymmetric  $n=0$  mode growth rates with resistive wall were obtained with the KINX-W code. A comparison shows that the axisymmetric stability of doublets is much better than that of a single axis plasma with the same overall elongation.

**1 Equilibrium** The equilibrium plasma boundary is chosen to obtain two magnetic axis equilibrium with prescribed profiles of the surface averaged toroidal current density  $I^*$  and  $\bar{dp}/d\psi$ . The following parameterization is suitable to generate a boundary with indentations from both inner and outer sides:

$$\begin{aligned} r &= R + a_i \cos(\theta + \delta_i \sin \theta)(1 - p_i \cos^2 \theta), & z &= Z + a\kappa_i \sin \theta, \\ i &= 1 \quad 0 < \theta < \pi, & i &= 2 \quad \pi < \theta < 2\pi. \end{aligned} \quad (1)$$

The values of  $\kappa_1, \delta_1$  and  $\kappa_2, \delta_2$  can be varied independently thus controlling the elongation and the triangularity of the upper and lower parts of the plasma cross-section. The relation  $a_1(1 - p_1) = a_2(1 - p_2)$  is needed to ensure the continuity of the shape.

For the profiles of  $I^*$  the following expression was chosen:

$$I^* = (1 - \psi^{j_1})^{j_2} + I_m, \quad (2)$$

where  $\psi$  is the normalized poloidal flux in each plasma subdomain with nested flux surfaces and  $I_m$  is chosen to ensure the continuity of  $I^*$  across subdomains boundaries.

To obtain a sequence of equilibria for  $\beta$ -limit computations we fix the profile of  $I^*$  and perform pressure gradient optimization to get the equilibrium marginally stable against ballooning modes. The  $\beta$ -limit for kink modes is obtained by rescaling the optimized  $\bar{dp}/d\psi$  profile until marginal stability is reached.

**2 External kink limits** The following plasma boundary parameters were chosen for up-down symmetric doublet configurations:  $a/R = 0.65, \kappa = 1.25, \delta = 0.1, p = 0.8$ , which gives the boundary aspect ratio  $A = 3.47$  and total elongation  $E = 2.89$ . This shape fits into the TCV vacuum vessel (Fig.2a). The mantle outside separatrix was chosen pressureless and currentless ( $I_m = 0$ ). The parameter  $j_2$  was fixed and the plasma current varied by changing  $j_1$  in equation (2). The value of  $q$  at the upper magnetic axis was set to 1.05 for all cases. In Fig.1a  $\beta$ -limits vs normalized current for  $j_2 = 1$  are shown. Note that the definitions here are  $\beta = 2 \int p dV / B_{vac}^2, I_N = I_p(MA) / a(m) B_{vac}(T)$

and the integrals are over plasma volume without mantle.  $B_{vac}$  is the vacuum field in the plasma centre. The same is shown in Fig.1b for the case  $j_2 = 2$  which corresponds to larger values of  $l_i$ . Maximum beta and current are somewhat higher in this case but the kink  $\beta$ -limit degradation is more pronounced when approaching the current limit.

The influence of the current in the mantle on the stability was studied by introducing  $I^* = I_m(1 - \psi)$  with  $I_m = 0.1, 0.2$  and  $j_2 = 1$  in plasma. The  $\beta$ -limits do not change much. But the current limit degrades with increasing  $I_m$ . In the table below limits in total current ( $I_{tot}$ ) and current inside separatrix ( $I_{int}$ ) are given.

$I_m$	0.0	0.1	0.2
$I_{tot}$	2.18	2.08	1.75
$I_{int}$	2.18	2.03	1.66

Comparing doublet plasmas (dt) with corresponding single-null plasmas inside separatrix taken alone (sn), it was found that the  $n=1$  external kink  $\beta$ -limit in doublets is about 5% lower than in single-null plasmas. The difference in current limit is even smaller. In the table below the beta limits are given for three types of current profiles.  $I_{Ndt}$  is the normalized current at the beta limit for doublets.

$j_1$	$j_2$	$I_m$	$\beta_{dt}$	$\beta_{sn}$	$I_{Ndt}$
1	1	0.0	2.1%	2.2%	1.00
1	1	0.1	2.6%	2.75%	1.16
2	2	0.0	2.7%	2.8%	1.06

**3 Up-down asymmetric doublets** Two examples of up-down asymmetric doublet equilibria were considered. The first one was obtained using the parameterization (1) with  $a_1/R = 0.65, a_2/R = 0.65, \kappa = 1.7, \delta = 0.1, p_1 = 0.85$  (Fig.2b). The current density profiles were  $I^* = 1 - \psi$  for the upper domain and  $I^* = 0.3(1 - \psi)$  for the lower domain. The flux outside separatrix is very small in this case (about 100 times smaller than inside the upper domain) and the separatrix closely follows the external boundary shape which has a low triangularity.

The second equilibrium boundary was obtained from the asymmetric "TCV-D" parameterization:

$$\begin{aligned}
 r &= R + a \cos(\theta + \delta \sin \theta - \lambda \sin 2\theta), & z &= a\kappa \sin \theta, \\
 \kappa &= 0.5(\kappa_1 + \kappa_2 + (\kappa_1 - \kappa_2) \sin \theta), \\
 \delta &= 0.5(\delta_1 + \delta_2 + (\delta_1 - \delta_2) \sin \theta), \\
 \lambda &= 0.5(\lambda_1 + \lambda_2 + (\lambda_1 - \lambda_2) \sin \theta), \\
 0 &< \theta < 2\pi.
 \end{aligned} \tag{3}$$

This shape with  $a/R = 0.3, \kappa_1 = 3.7, \kappa_2 = 1.7, \delta = 0.5, \lambda = 0.2$  was indented from both inner and outer sides by  $0.3a$  and  $a$  respectively (Fig.2c). The current density was  $I^* = 1 - \psi$  for both upper and lower domains.

The ballooning  $\beta$ -limit is higher for the second case of Fig.2c because of its more triangular boundary ( $g = \beta/I_N = 2.75\%/0.76 = 3.6\%$  for Fig.2b vs  $g = \beta/I_N = 3.5\%/0.81 = 4.3\%$  for Fig.2c; the values are computed over upper domains only, lower domains were kept force-free). The same holds for the kink limit ( $g = 3.0\%$  vs  $g = 4.2\%$ ). Again no substantial differences were revealed between the kink limits for doublets and single-null plasmas.

**4 Axisymmetric stability** A wall shape close to that of TCV vacuum chamber was chosen for  $n=0$  stability studies (using the parameterization (3) with  $a/R =$



$a_w/R_w = 0.34, \kappa = 2.7, \delta = 0.2, \lambda = 0.8$ ). Two versions of the KINX-W code were used to compute the growth rates of doublet and single axis equilibria surrounded by the resistive wall.

Four equilibria with  $\beta = 0$  were compared : a symmetric doublet (Fig.2a) with  $I^* = 1 - \psi, I_N = 1.15$ , two asymmetric doublets Fig.2b and 2c with  $I_N = 0.90$  and  $I_N = 1.24$  and a single axis highly elongated equilibrium of "TCV-D" shape (Fig.2d) with  $R/a = 3.67, \kappa = 3, \delta = 0.5, \lambda = 0.2, I^* = 1 - \psi, I_N = 2.07$ .

The table below shows the instability growth rates in  $s^{-1}$  obtained assuming the plasma major radius  $R=0.88m$  and a resistivity/wall thickness ratio of  $10^{-5}Ohm$  (the growth rates scale linearly with increasing the resistivity up to  $5 \cdot 10^{-5}$  which is closer to the experimental value). The resistive growth rates for doublets (first two rows in

	sym. doublet (a)	asym. doublet (b)	asym. doublet (c)
doublet (1)	44	62	360
doublet (2)	28	ideally unstable	27
single top	43	62	800

the table) and for the corresponding single-null plasmas from the upper domains inside separatrix (single top) are close to each other in the two first cases where the separatrix is near the external boundary at the top. For the asymmetric doublet (c) the growth rates are higher due to a more triangular boundary which is not following the wall shape like in the two other cases. The stabilizing influence of the plasma outside the separatrix is considerable in this case and the growth rate for the single-null plasma is much higher than for the doublet.

A characteristic feature of  $n=0$  stability of up-down symmetric doublets is the presence of two unstable modes [1]. The same is valid for the resistive wall modes: for the most unstable mode the displacements in the two domains inside the separatrix are mirror symmetric, the plasma is displaced mainly as a whole for the more stable mode. The growth rates of the two modes are close to each other for the symmetric doublet. For asymmetric doublets the two modes are mainly independent displacements of each domain inside the separatrix. For the asymmetric doublet (b) the plasma in the lower smaller domain is ideally unstable due to its relatively high elongation and large distance from the wall. For the asymmetric doublet (c) the mode in the lower domain is ideally stable and has a much lower resistive growth rate because its shape follows the wall more closely.

For the TCV wall position with  $a_w/R_w = 0.34$  the highly elongated equilibrium is ideally unstable. Even for a wall with  $a_w/R_w = 0.31$  the growth rate is much higher than for the doublets:  $1300s^{-1}$ .

**5 Conclusions** Comparisons of the  $\beta$  and current limits against external  $n=1$  kink stability for doublets and for corresponding single-null plasmas inside the separatrix show that the limits are very close to each other. No substantial influence of the mantle on the stability was revealed.

The maximal  $\beta$  obtained for doublet configurations is almost the same as for plasmas having a single axis and the same overall elongation. The current limit for the doublet imposed by  $n=1$  external kink mode appears to be lower by 30%. But the optimum  $\beta$  [2] is obtained at approximately the same current.

The  $n = 0$  mode stability properties of doublet equilibria can be influenced by the plasma outside the separatrix. The displacements for the two unstable modes in asymmetric doublets are localized in either one or the other domain inside the separatrix. However the interaction between the plasma domains can be considerable. A comparison shows that the  $n=0$  mode growth rate with resistive wall stabilization are much lower for doublets than for a single axis plasma with the same overall elongation.

**Acknowledgement** This work was partly supported by the Fonds National Suisse de la Recherche Scientifique.

## References

- [1] Medvedev S., Villard L., Degtyarev L.M., Martynov A., Gruber R., Troyon F. MHD equilibrium and stability of doublet configurations. 20th EPS Conf. on Controlled Fusion and Plasma Phys., Lisbon, Proc. Contrib. Papers vol.IV (1993) 1279
- [2] Jardin S.C. *et al.*, MHD constraints for advanced tokamak operation Proc. 14th Conf. Plasma Phys. Controlled Nucl. Fusion Research, Würzburg, vol.2 (1992) 285

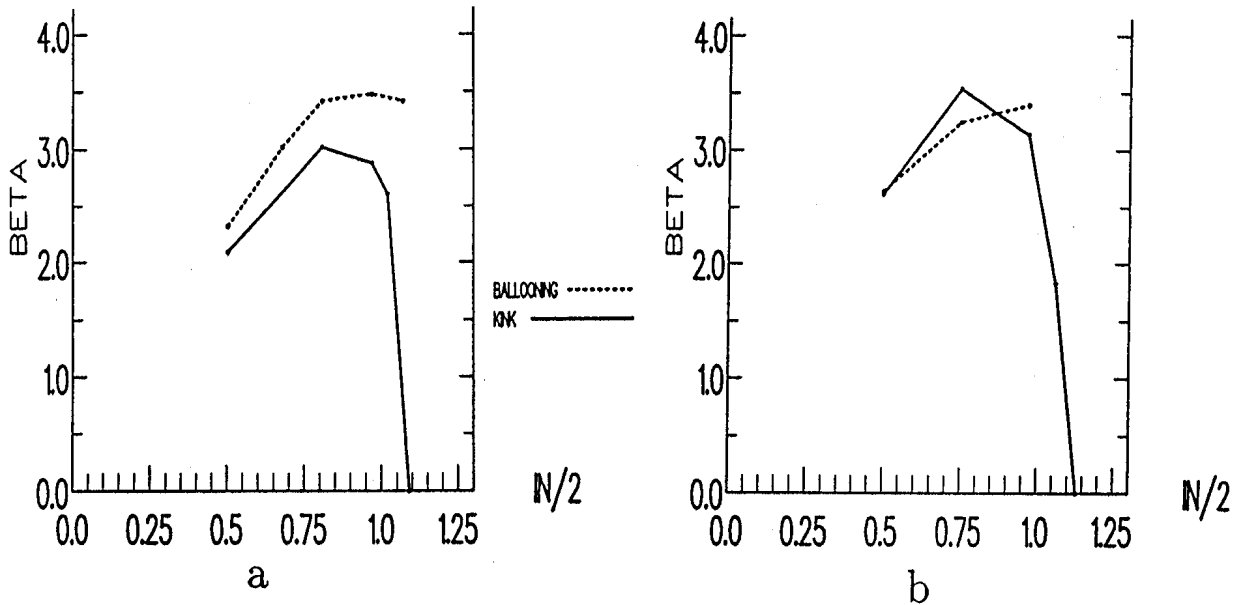


Figure 1: Ballooning and kink limiting values of  $\beta$  vs half of the normalized current inside separatrix: (a) current density parameter  $j_2 = 1$  (b)  $j_2 = 2$ .

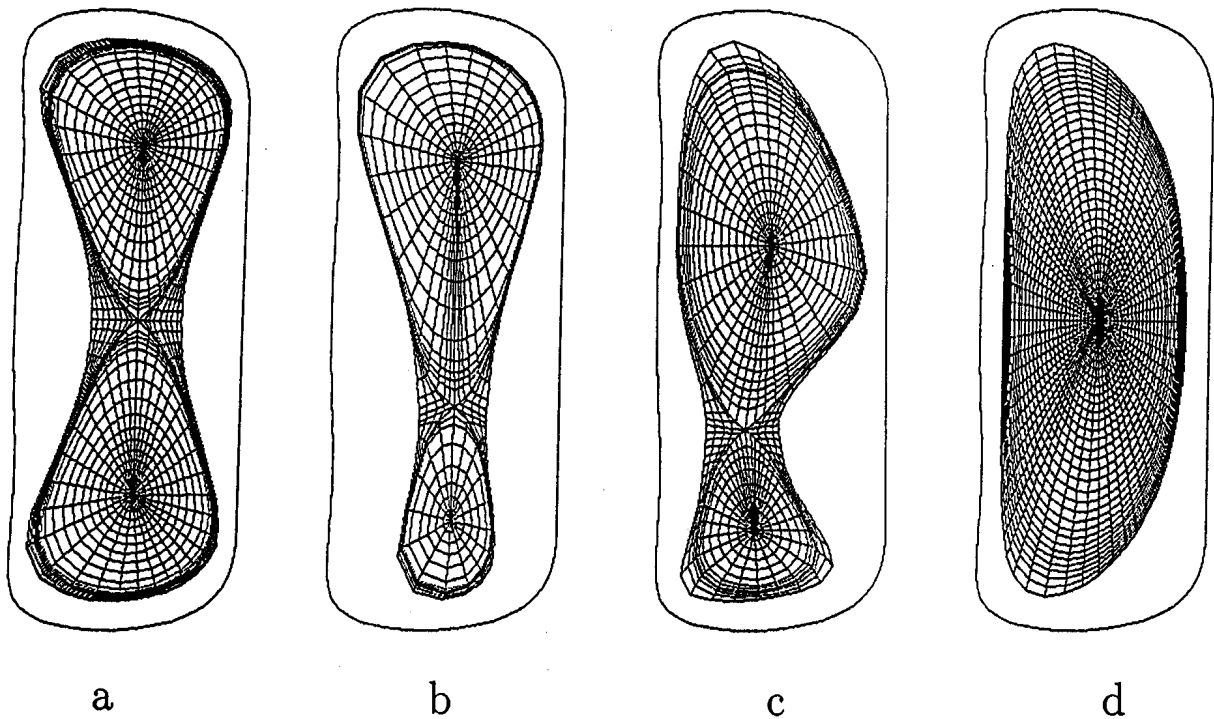


Figure 2: Equilibrium grid adapted to magnetic surfaces inside the wall: (a) symmetric doublet (b) asymmetric doublet (c) asymmetric doublet (d) highly elongated single axis equilibrium.

## Stabilization of Pressure-Driven External Modes in Tokamaks with a Resistive Wall and Toroidal Rotation

D. J. Ward<sup>a</sup> and A. Bondeson<sup>a,b</sup>

<sup>a</sup>Centre de Recherches en Physique des Plasmas,

Association Euratom-Confédération Suisse, EPFL, Lausanne

<sup>b</sup>Dept. of Technology, Euratom-NFR Association, Uppsala University, Uppsala, Sweden.

In recent work [1], we have shown that it is possible to completely stabilize low  $n$ , pressure-driven external modes in tokamaks by the combined effect of resistive walls and toroidal plasma rotation. We have used numerical computation to study the wall stabilization in toroidal geometry. The spectral codes MARS [2] and NOVA [3] have been modified to include a resistive shell in the vacuum region surrounding the plasma. Rigid toroidal rotation was modeled by making the resistive shell rotate with an externally imposed frequency  $\omega_{\text{rot}}$  while the equilibrium was static. The plasma was treated as ideally conducting and  $\omega_{\text{rot}}$  was some fraction of the sound frequency. Furthermore, the time-constant of the resistive wall,  $\tau_w$ , was taken much larger than any ideal-MHD timescale.

Sonic rotation complicates the stability problem by coupling to sound waves, for which the MHD model predicts an unphysical resonant behavior. For realistic temperature ratios, the sound waves are strongly damped by ion Landau damping, and an accurate calculation requires a description that is kinetic along the field lines. However, reasonable approximations of the kinetic behavior can be obtained by adding dissipative terms to the fluid equations. We have applied three such modifications of the scalar-pressure ideal MHD equations. Two of these consist of adding a damping term for the Lagrangian pressure perturbations. The perturbed pressure is split into a convective and a Lagrangian part:

$$p_1 = -\vec{\xi} \cdot \nabla p_0 + p_{1L}, \quad \text{where} \quad \partial p_{1L} / \partial t = -\Gamma p_0 \nabla \cdot \vec{v} - \nu p_{1L} \quad (1)$$

The damping rate  $\nu$  is taken either to be a fixed number or to represent a thermal diffusivity following the Hammet-Perkins [4] prescription,  $\nu = \chi |k_{\parallel} v_{\text{thi}}|$ . As a third alternative, we use a term representing parallel viscosity in the equation of motion along the field lines so that  $v_{\parallel} \equiv (\vec{B}_0 / B_0) \cdot \vec{v}$  is computed from

$$\partial v_{\parallel} / \partial t = -(\vec{B} \cdot \nabla p)_1 / B_0 \rho_0 - \kappa |k_{\parallel} v_{\text{thi}}| v_{\parallel} \quad (2)$$

When the pressure exceeds the stability limit with the wall at infinity, we find two classes of modes that can potentially be unstable: (a) one which has zero frequency in the frame of the plasma and hardly penetrates the resistive wall: the "plasma mode"; and (b) one which penetrates the wall and rotates slowly with respect to it (slip frequency =  $O(\tau_w^{-1}) \ll \omega_{\text{rot}}$ ): the "resistive wall mode." The resistive wall mode rotates with respect to the plasma at a frequency close to the imposed rotation frequency. A typical example of how the growth rates of the plasma and resistive wall modes depend on the wall radius  $d$  is shown in Fig. 1. The two modes are influenced in opposite ways by the wall distance—the plasma mode is *destabilized* as the wall is moved further from the plasma, while the resistive wall mode is *stabilized*.

The plasma mode rotates quickly (frequency  $\approx \omega_{\text{rot}} \gg \tau_w^{-1}$ ) with respect to the wall. It does not penetrate the wall and behaves as if the wall were ideal. The plasma mode is

unstable on the ideal MHD time scale when the wall radius exceeds the usual ideal MHD threshold for wall stabilization,  $d_{\text{ideal}}$ . This marginal wall position approaches infinity at the conventional beta limit and decreases with increasing pressure.

The resistive wall mode becomes increasingly stable with increasing wall radius. This counter-intuitive behavior can be understood by a large-aspect-ratio calculation of  $\Delta'_w$  at the resistive shell. We consider a magnetic perturbation in the vacuum, dominated by one poloidal harmonic  $m$  (assumed  $> 0$ ). The perturbed magnetic flux function  $\psi$  satisfies  $\nabla_{\perp}^2 \psi = 0$  in the vacuum region, and the poloidal harmonic  $m$  is a linear combination of  $r^{-m}$  and  $r^m$ . The growth rate of the resistive wall mode is given by  $\gamma = \tau_w^{-1} d \Delta'_w$ , where  $\Delta'_w = [\psi'(d_+) - \psi'(d_-)]/\psi(d)$ . If we write the logarithmic derivative of  $\psi$  at the plasma edge  $r = a$  as  $(\psi'/\psi)_{r=a} = -(m/a)(1+z)$  (with  $z = x + iy$ ,  $x$  and  $y$  real and  $y \neq 0$  because of the rotation) a simple calculation gives  $\Delta'_w$ :

$$d\Delta'_w/2m[1 - (a/d)^{2m}] = z/(w - z) = [(wx - x^2 - y^2) + iwy]/[(w - x)^2 + y^2] \quad (3)$$

where  $w = 2/[(d/a)^{2m} - 1]$ . In the case with no rotation ( $y = 0$ ) and the plasma unstable in the absence of a wall ( $x > 0$ ), Eq. (3) shows that the resistive wall mode is unstable ( $\Delta'_w > 0$ ) for  $a \leq d < d_{\text{ideal}} \equiv a[1+2/x]^{1/2m}$ . As the wall radius increases,  $\Delta'_w \rightarrow \infty$  when  $d \rightarrow d_{\text{ideal}}$ , and at this wall position, the resistive wall mode connects to the ideal MHD instability, which occurs for  $d > d_{\text{ideal}}$ . In the region of ideal instability, plasma inertia is non-negligible and modifies  $(\psi'/\psi)_{r=a}$  so as to keep  $\Delta'_w \approx +\infty$ . When the rotation frequency is finite,  $y$  is non-zero. This eliminates the zero in the denominator of Eq. (3). Consequently,  $\Delta'_w$  remains finite and complex for all wall distances, and the resistive wall mode does not join the ideal instability. Rotation effectively separates the resistive wall mode from the plasma mode, and the growth rate of the resistive wall mode remains  $O(\tau_w^{-1})$  for all  $d$ . The resistive wall mode is stabilized when  $d_{\text{res}} > a[1+2x/(x^2+y^2)]^{1/2m}$ .

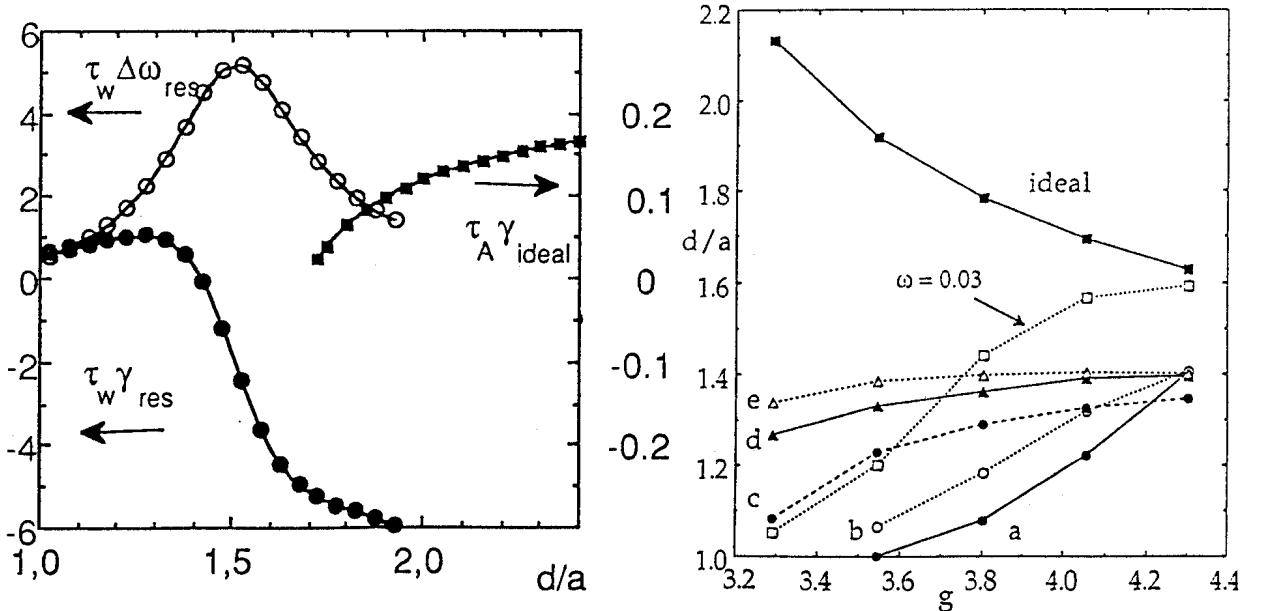


Figure 1: Growth rate  $\gamma_{\text{res}}$  and slip frequency  $\Delta\omega_{\text{res}}$  vs. wall radius for  $\omega_{\text{rot}}/\omega_A = 0.06$ . Figure 2: Marginal wall distance versus Troyon factor  $g$  for the plasma mode (marked "ideal") and the resistive wall mode using different assumptions. Curves (a)–(e) apply for  $\omega_{\text{rot}}/\omega_A = 0.06$ . (a) and (b) give results for the pressure damping model, Eq. (1), with (a)  $\nu/\omega_A = 0.025$  and (b)  $\nu/\omega_A = 0.0025$ . (c)–(e) give results for the parallel viscosity model Eq. (2) with (c)  $\kappa = 0.1$ , (d)  $\kappa = 0.885$ , and (e)  $\kappa = 1.77$ .

Thus, when a rotating plasma exceeds the pressure limit with the wall at infinity, there are two stability limits for the wall radius,  $d_{\text{res}}$  and  $d_{\text{ideal}}$ . The plasma is stable when  $d_{\text{res}} < d < d_{\text{ideal}}$ , and this condition must apply for all  $n$  (except  $n = 0$ , which is usually stabilized by active feedback on the resistive shell time scale). We have computed stability limits, including rotation and resistive walls, for several MHD equilibria. Generally, the effect of wall stabilization is stronger when the pressure profile is broad so that the beta limit is set by external modes. An example is given in Fig. 2, which shows  $d_{\text{ideal}}$  and  $d_{\text{res}}$  versus normalized pressure  $g$  for  $n = 1$  and rotation frequency  $\omega_{\text{rot}}/\omega_A = 0.06$ . The computations were made for an equilibrium with JET shape (elongation = 1.7, triangularity = 0.3 and aspect ratio = 3) and a low pressure peaking factor,  $p_0/\langle p \rangle \approx 1.7$ . The current profile was adjusted to keep  $q_0 = 1.2$  and  $q_s = 2.55$ . The resistive shell was conformal with the plasma boundary and we used different fluid approximations to show the dependence on model assumptions. Stability limits are shown for the  $n = 1$  resistive wall mode using the model of Eq. (1) with  $\nu/\omega_A = 0.0025$  and  $\nu/\omega_A = 0.025$  and the parallel viscosity model Eq. (2) with  $\Gamma = 1.5$  and  $\kappa = 1.77, 0.885$  and  $0.1$ . The Hammett-Perkins approximation with  $\chi = 2/\pi$  gives a result almost identical to that for the pressure damping model with  $\nu/\omega_A = 0.025$ . Thus, the two pressure damping models of Eq. (1) give rather similar results, while the parallel viscosity model gives a stronger stabilizing effect. Furthermore, if the sound waves are eliminated by setting  $\Gamma = 0$ , the wall stabilization becomes much weaker. We conclude that the stabilization by resistive walls and rotation is sensitive to the dynamics of sound waves and an accurate theory must be kinetic along the field lines (e.g., drift kinetic).

Also shown in Fig. 2 is a comparison case with half the rotation frequency,  $|\omega_{\text{rot}}/\omega_A| = 0.03$  (and  $\Gamma = 1.5, \kappa = 1.77$ ). The stabilization is much weaker for this lower rotation frequency and is almost lost when  $\omega_{\text{rot}}/\omega_A \leq 0.02$ . Thus, there is a threshold behavior with respect to the rotation frequency. For this type of equilibrium,  $\omega_{\text{rot}}/\omega_A$  needs to be about 0.05 to give a significant stabilizing effect. This corresponds to a minimum rotation frequency of about 20% of the sound frequency at the  $q = 2$  surface.

We find that when  $q_s$  is increased (holding the pressure profile fixed),  $d_{\text{res}}$  for  $n = 1$  moves closer to the plasma boundary, and the maximum normalized beta is increased. Figure 3 shows the regions of stability with  $q_s = 2.55$  and  $q_s = 3.55$  for equilibria with identical pressure profiles and  $q_0$  fixed at 1.20. The stability calculations are performed with the constant damping model and different damping coefficients. The stability limit, when expressed in terms of normalized beta, is higher at  $q_s = 3.55$  than at  $q_s = 2.55$  for both the resistive wall and the plasma mode. Increasing  $q_s$  to higher values further increases the stable  $g$ . We have also examined equilibria with negative central shear and high bootstrap fraction, similar to those discussed in [5]. For these equilibria, with peaked pressure profiles and only one integer- $q$  surface ( $q = 3$ ), wall stabilization is not very effective. However, even rather small modifications of the equilibrium profiles, with an increased pressure gradient close to the edge and a somewhat larger region of positive

files and high  $q_s$ . A numerical example with standard  $q$ -profile and broad pressure profile shows an increase in the beta limit by about 30% due to the wall stabilization. MHD stability analyses indicate that similar increases are observed experimentally in DIII-D [6]. Stabilization by resistive walls and rotation can give even more favorable results for advanced tokamak operation (non-monotonic  $q$  and  $\approx 100\%$  bootstrap fraction), but for such equilibria, global stability becomes sensitive to edge conditions.

ACKNOWLEDGMENT

This work was supported in part by the Swiss National Science Foundation.

REFERENCES

- [1] A. Bondeson and D. J. Ward, Phys. Rev. Lett. **72** (1994) 2709.
- [2] A. Bondeson, G. Vlad, and H. Lütjens, Phys. Fluids **B 4** (1992) 1899.
- [3] C. Z. Cheng and M. S. Chance, J. Comput. Phys. **71** (1987) 124; D. J. Ward, S. C. Jardin, and C. Z. Cheng, J. Comput. Phys. **104** (1993) 221.
- [4] G. W. Hammett and F. W. Perkins, Phys. Rev. Lett. **64** (1990) 3019.
- [5] C. Kessel, et al., Phys. Rev. Lett. **72**, (1994) 1212.
- [6] A. D. Turnbull, et al., Int. Sherwood Theory Conf., Dallas, TX, 1994, paper 2B1.

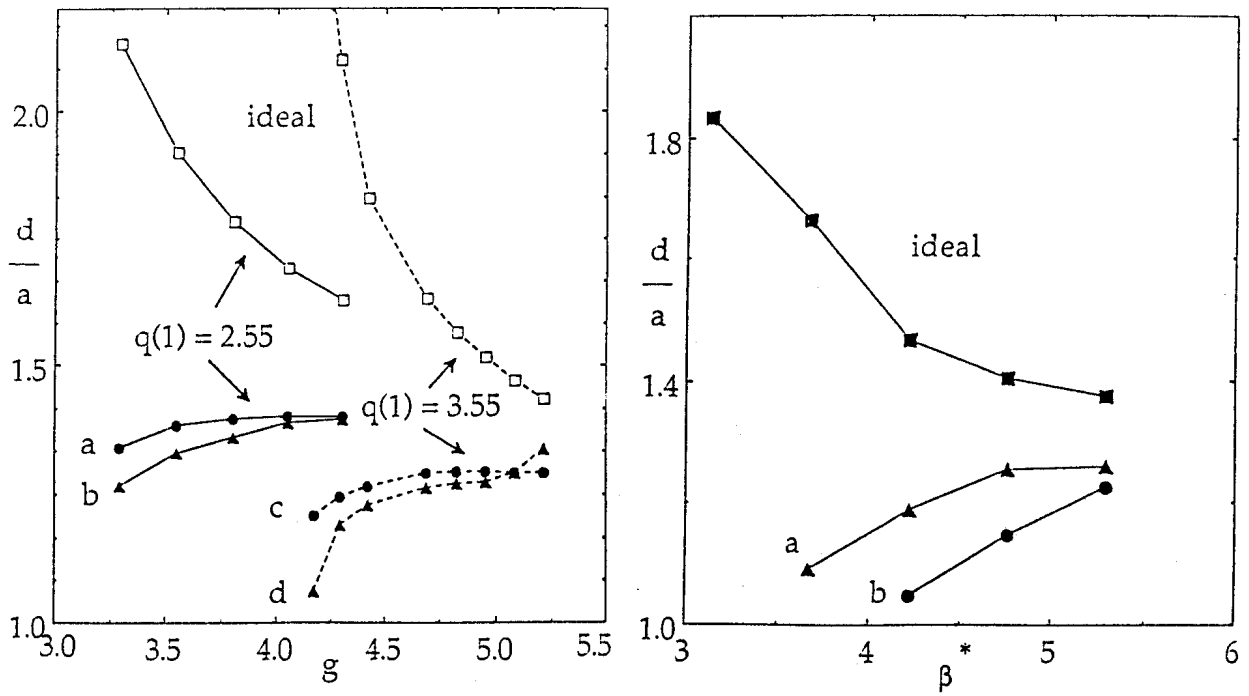


Figure 3: Marginal wall distance versus Troyon factor  $g$  for equilibria with the same pressure profile, with  $q_s = 2.55$  and  $q_s = 3.55$ . (a)–(b) are the resistive wall modes for  $q_s = 2.55$  with the pressure damping model, Eq. (1), with (a)  $\nu/\omega_A = 0.025$  and (b)  $\nu/\omega_A = 0.0025$ . (c) and (d) are resistive wall modes for  $q_s = 3.55$  equilibria with (c)  $\nu/\omega_A = 0.025$  and (d)  $\nu/\omega_A = 0.01$ .

Figure 4: Stability boundaries for equilibria with negative central shear and high bootstrap fraction. Results are shown for (a) the pressure damping model, Eq. (1), with  $\nu/\omega_A = 0.35$ , and (b) the parallel viscosity model with  $\kappa = 1.77$ .

# Tearing stability of an ITER shaped plasma

A. Pletzer, J. Manickam\*, and D.A. Monticello\*  
*Centre de Recherches en Physique des Plasmas*  
*Association Euratom – Confédération Suisse*  
*Ecole Polytechnique Fédérale de Lausanne*  
*21 Av. des Bains, CH-1007 Lausanne, Switzerland*  
 \* *Plasma Physics Laboratory, Princeton University*  
*Princeton, New Jersey 08544, USA*

## 1. Introduction

The focus of the present paper is to present calculations of the nonideal stability index  $\Delta'$  using the toroidal axisymmetric code PEST-3 [1], which has recently been upgraded to treat plasmas with an up-down asymmetric cross-section. In the case of the ITER tokamak, this up-down asymmetry is due to the presence of a single magnetic divertor.

The code PEST-3 solves the ideal MHD marginal stability equation in the plasma bulk. The inner layers located at the  $q = m/n$  rational surfaces appear as singularities. These are resolved as a separate problem involving nonideal physics. A variational principle is exploited to determine the coefficients of the recessive or “small” singular solutions normalized to the “large” singular solutions. Because we allow for the presence of  $N > 1$  rational surfaces for a given toroidal mode number  $n$ ,  $\Delta'$  generalizes to a matrix  $\Delta'_{ij}$  where  $i, j = 1, 2 \dots N$ . For the sake of generality, we also compute the matching data  $A'_{ij}$ ,  $B'_{ij}$  and  $\Gamma'_{ij}$  [2] which are associated with the coupling of tearing parity to interchange parity modes. These data are only important when  $\Delta'$  is large or when  $D_{I,i}$ , the Mercier function at the rational surface  $\psi = \psi_i$ , differs significantly from the critical zero- $\beta$  value of  $-1/4$  for which the mode has a pure tearing parity (and for which the constant  $\Psi$  approximation is particularly adequate). These matching data are conveniently assembled to form the *outer region matching matrix*

$$D' \equiv \frac{1}{2} \begin{pmatrix} A' & B' \\ \Gamma' & \Delta' \end{pmatrix}, \quad (1)$$

which condenses all the outer region information necessary to match the singular solutions to arbitrary inner layer solutions. It is apparent from the expression of  $D'$  in terms of small and large solutions, Eq.(46) in Ref. [3] or Eq.(99) in Ref. [1], that  $D'$  is symmetric for real singular solutions and that we must have  $D'^t = D'$  in the case of up-down asymmetry. This property is confirmed numerically.

To the outer region matching matrix  $D'$  corresponds, in the linear theory, an inner layer matching matrix  $D(\gamma)$ . The matching condition then takes the form of a dispersion relation  $\det[D' - D(\gamma)] = 0$ , which is used to extract the growth rates  $\gamma$ 's by scanning in the complex plane. In small  $\beta$  plasmas, we have  $|A'| \gg |B'| \sim |\Gamma'| \gg \Delta'$ , so that the dispersion relation can often be simplified to  $\det[\Delta' - \Delta(\gamma)] = 0$ . Furthermore it is well known that in the linear zero- $\beta$  theory of tearing modes [4],  $\Delta \sim \gamma^{5/4}$ , so that the dispersion relation immediately gives the condition that  $\Delta'$  be negative definite for stability. This criterion remains valid in the collisionless limit [5,6], but becomes only

sufficient when pressure gradient and compressibility are accounted for [7] and when the resistive Mercier function  $D_{R,i} < 0$ . Rutherford [8] showed that in the nonlinear regime, the magnetic island width grows proportionally to  $\Delta'$  and more recently, Waelbroeck [9] and Zakharov *et al.* [10] have shown that  $\lambda_H \equiv \pi/\Delta'$  provides the basic matching condition to resolve the helical near equilibrium, magnetic configuration of the inner layer, which is thought to develop in the early nonlinear stage of sawtooth reconnection.

## 2. $\Delta'$ and linear resistive growth rates

We perform the matching of the tearing parity solutions arising in the ITER plasma shown in Fig. 1, to the resistive inner solutions of Glasser *et al.* [7]. In this case, we have the diagonal matrix

$$\Delta(\gamma) = \left( \frac{\Delta_i(\gamma)}{2\mu_i L_i^{2\mu_i}} \delta_{ij} \right), \quad (2)$$

and

$$\Delta_i(\gamma) = 2^{2\mu_i} \pi \frac{\Gamma(\frac{3}{4})}{\Gamma(\frac{1}{4})} \hat{Q}_i^{5/4} \left( 1 - \frac{\pi D_{R,i}}{4\hat{Q}_i^{3/2}} \right) \quad (3)$$

as inner matching data defined in the inner layers  $i = 1, 2 \dots N$ , where

$$\hat{Q}_i \equiv \gamma/Q_i \quad (4)$$

is the normalized growth rate, and  $\mu_i \equiv \sqrt{-D_{I,i}}$  is assumed to be real by virtue of Mercier's criterion. Expressions for  $D_{I,i}$ ,  $D_{R,i}$ , the characteristic growth rate  $Q_i$  and the layer width  $L_i$  are given by Eqs.(139)–(149) in Ref. [1]; they depend entirely on the equilibrium quantities evaluated at given flux coordinates. Recall that  $Q_i$  and the layer width  $L_i$  scale as the resistivity  $\eta$  to the power 1/3. A direct consequence of (2) and (3) plus the fact that  $D'$  is Hermitian is that the growth rates always come as complex conjugate pairs.

The safety factor profile is monotonically increasing from  $q_0 = 1.1$  to  $q_a = 3.1$ , yielding two rational surfaces,  $m = 2/n = 1$  and  $m = 3/n = 1$ , which are located at 0.89% and 0.99% of the plasma boundary flux  $\psi_a$ , respectively. Figure 2 shows the convergence of the two eigenvalues  $\lambda_{2/1}$  and  $\lambda_{3/1}$  of the  $\Delta'$  matrix. The boundary conditions applied on the displacement field are those of an infinitely conducting wall at the plasma surface ( $b = a$ ), at distance  $b = 1.2$  times the plasma boundary radius  $a$  and at infinity. The destabilizing effect of increasing  $b$  is particularly noticeable for the 3/1 tearing mode, which remains nevertheless stable (negative eigenvalue) even after complete removal of the wall. The 2/1 mode has a marginally positive eigenvalue  $\lambda_{2/1} = 0.209$  for the fixed boundary case whereas  $\lambda_{2/1} = 0.532$  for  $b = 1.2a$  and  $\lambda_{2/1} = 3.58$  for  $b \rightarrow \infty$ .

Due to finite pressure gradient effects ( $D_{R,1} = -0.0027$ ), the instability only occurs when the eigenvalue exceeds a threshold  $\Delta_c$  which increases as  $\eta$  decreases. This leads to complete stabilization for  $\eta < \eta_c$ , where  $\eta_c$  ranges from  $10^{-6}$  to  $10^{-9}$  depending on the boundary conditions. There is a second branch in the dispersion relation which gives a much smaller growth rate (not shown). As  $\eta$  decreases, this branch however merges to the dominant one to form two complex conjugate growth rates. The particular value of  $\eta$  where this takes place is made apparent by the abrupt rise of the imaginary part (only one complex root is shown).



### 3. Summary

The latest PEST-3 version for plasmas with up-down asymmetric cross-section has



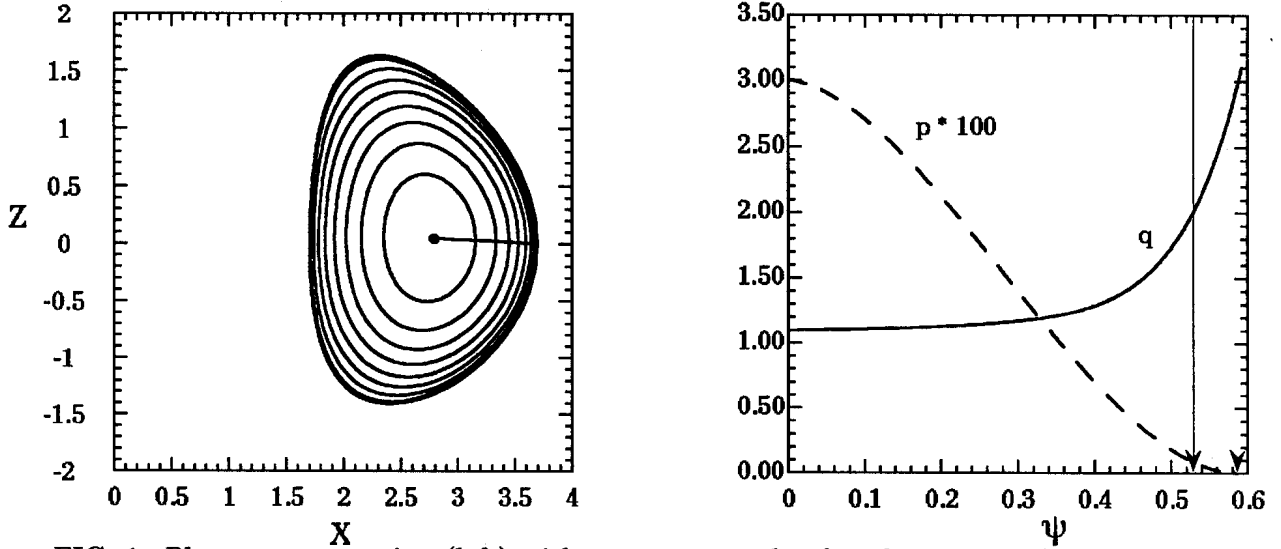


FIG. 1. Plasma cross-section (left) with pressure  $p$  and safety factor  $q$  profiles vs the flux coordinate  $\psi$  (right). The two vertical arrows indicate the positions of the  $q = 2/1$  and  $q = 3/1$  surfaces. The values for the inverse aspect ratio, the ellipticity, the triangularity and the average  $\beta \equiv 2p/B^2$  are  $\epsilon = 0.36$ ,  $E = 1.43$ ,  $T = 0.32$  and  $\langle \beta \rangle = 2.13\%$ , respectively.

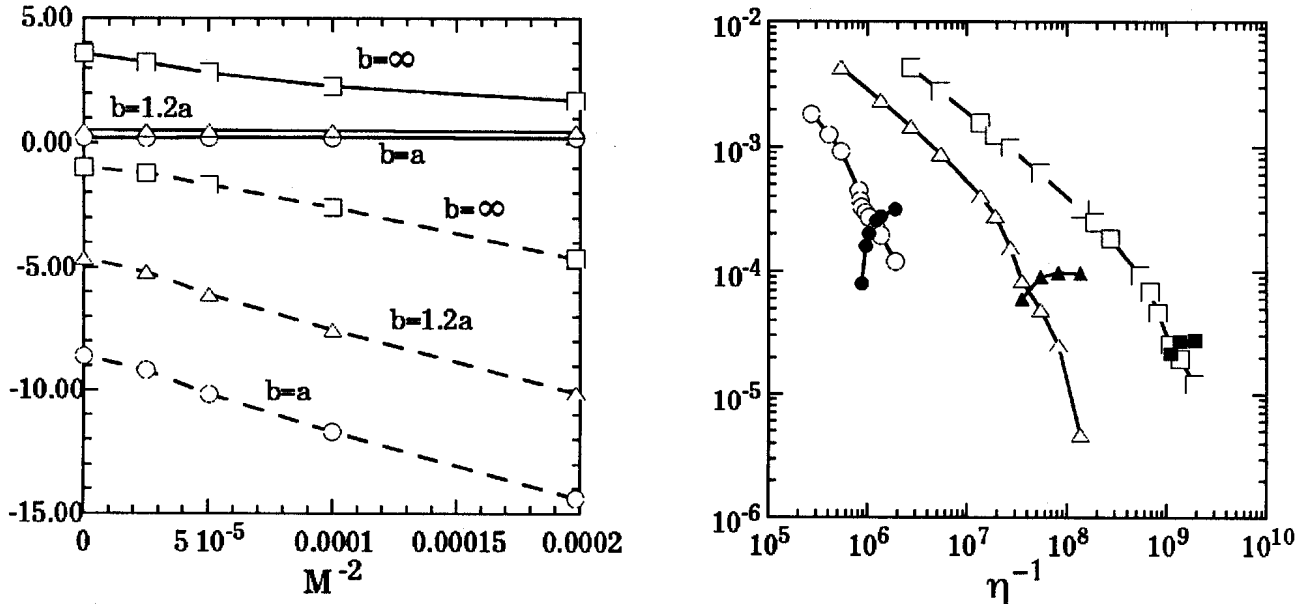


FIG. 2. Convergence of the two eigenvalues of  $\Delta'$  vs the inverse square of the number of radial mesh nodes  $M$  (left) and dominant growth rates vs the inverse resistivity  $\eta$  (right). The growth rates are normalized to the Alfvén frequency. The boundary conditions are  $b = a$  (circles),  $b = 1.2a$  (triangles) and infinite vacuum (squares). Closed symbols refer to the imaginary part of the growth rates.

## MHD-activity in Ohmic, Diverted and Limited H-mode Plasmas in TCV

A. Pochelon, M. Anton, F. Bühlmann, M.J. Dutch, B.P. Duval, A. Hirt,  
F. Hofmann, B. Joye, J.B. Lister, X. Llobet, Y. Martin, J.M. Moret,  
Ch. Nieswand, A.Z. Pietrzyk, G. Tonetti and H. Weisen.

Centre de Recherches en Physique des Plasmas  
Ecole Polytechnique Fédérale de Lausanne  
Association Euratom-Confédération Suisse  
21 Avenue des Bains, CH-1007 Lausanne, Switzerland

### Introduction



measurements using one vertical and one horizontal 20-channel camera (fig. 2). The center of gravity of the X-ray emission rotates with an excursion radius of normally 5-10 mm (up to 20 mm in some high density limiter H-modes). The modes slow down within 5-20 ms from initially  $\sim 5$  kHz, as is characteristic of sawtooth precursors, until they become quasi-stationary or lock. Locking is followed by a disruption within 2-20 ms. The disruptions are often partial and are followed by a transient recovery, despite the persistence of a large locked or rotating mode. In some cases disruptions have also been observed while the mode was still rotating.

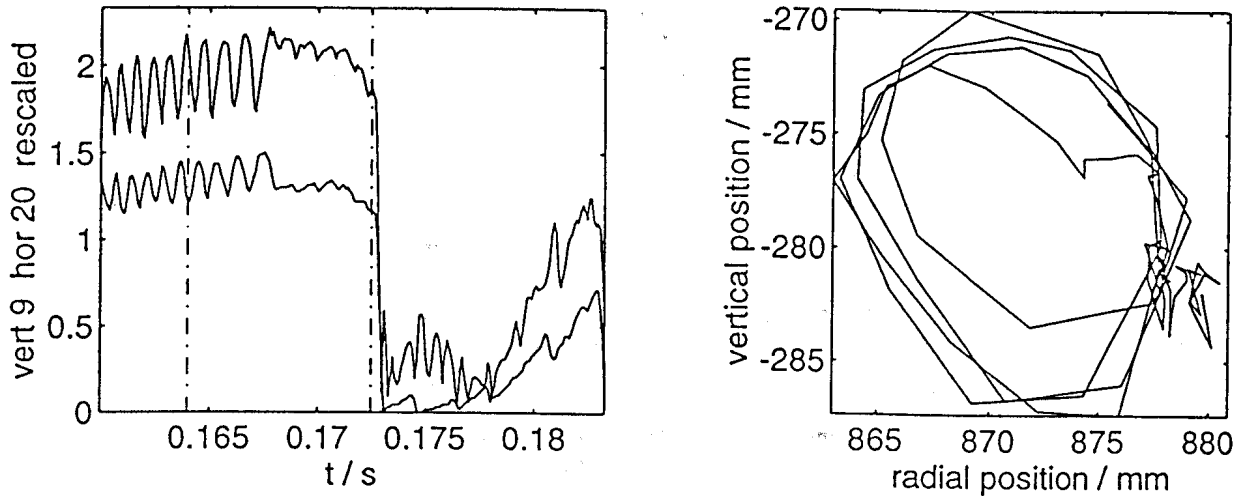


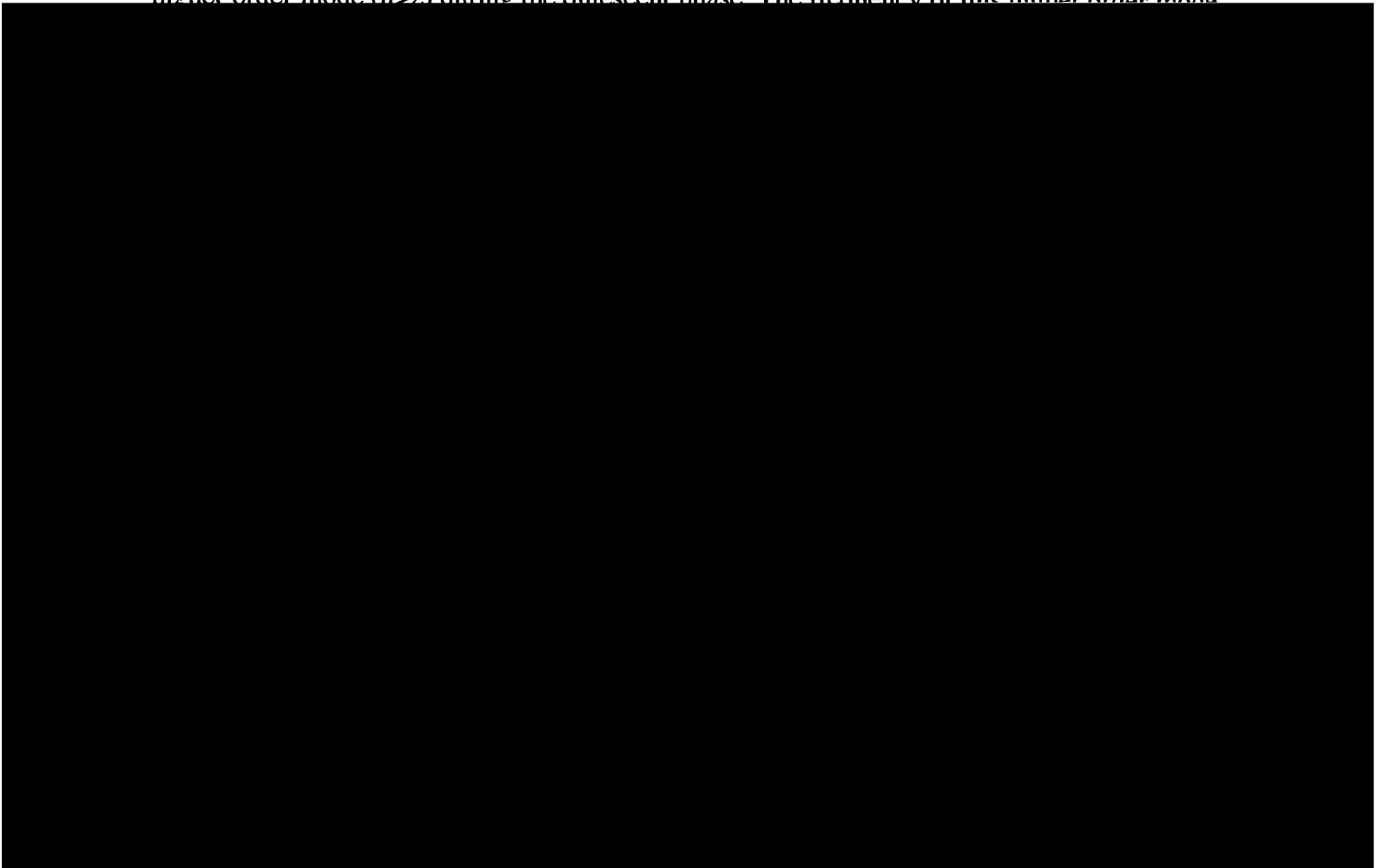
**Fig.2** Locked mode and partial disruption a) X-ray signals b) Trajectory of emission centroid.

For most locked modes the magnetic structure obtained from difference measurements using probes in toroidally opposite sectors exhibits a clear odd-n (presumably  $n=1$ ),  $m=2$  mode even when  $q_{95} > 3$ . Mode amplitudes at the probe locations range from  $5 \times 10^{-3}$  T after initial

the plasma periphery increases dramatically in the H-mode, resulting in a stair-case like increase of X-ray emission and thus electron pressure indicating the formation of an edge transport barrier. Large ELMs cause a sudden drop of the edge density and X-ray emissivity indicative of a rapid loss of edge pressure (fig. 3d). Large ELMs produce characteristic magnetic signatures, the strongest of which are observed on magnetic probes in the vicinity of the X-points. In diverted H-modes the magnetic signals of a significant number of large ELMs are detected within a few hundred  $\mu\text{s}$  of a sawtooth crash. Interestingly, large ELMs have also been observed to precede the crash in diverted H-modes.

A number of diverted discharges exhibit grassy ELMs appearing as small modulations of the  $D_\alpha$  signal around its level in the quiescent H-mode. These ELMs are observed at line average densities between  $5 \times 10^{19} \text{ m}^{-3}$  and  $1.6 \times 10^{20} \text{ m}^{-3}$  and their occurrence is uncorrelated with the sawtooth crashes. At the lower densities, the repetition rate gradually increases with density (from 200 Hz to 3 kHz) as the H-mode progresses, while at high density the grassy ELM occurrence becomes stochastic. Unlike large ELMs, grassy ELMs do not prevent the density rise. Fast MHD bursts coincident with the  $D_\alpha$ -rise phase of these grassy ELMs have been observed, and may be responsible for these modulations of the recycling (fig. 4).

The most striking change in magnetic activity at the transition is the order-of-magnitude reduction both of the level of broadband turbulence and of the amplitude of the coherent  $n=1$  mode (when observable) often associated with sawtooth activity (fig. 5). This reduction is not due to an increase of the plasma-probe distance. In diverted H-modes, the  $n=1$  mode sometimes disappears entirely, reappearing in some cases as bursts synchronized with the sawtooth cycle. More subtle changes have also been noted, such as the reduction of the frequency of  $n=1$  modes from  $\sim 5$  kHz to  $\sim 1$  kHz prior to the transition and the appearance of a higher order mode ( $n > 2$ ) during the quiescent phase. The frequency of this higher order mode



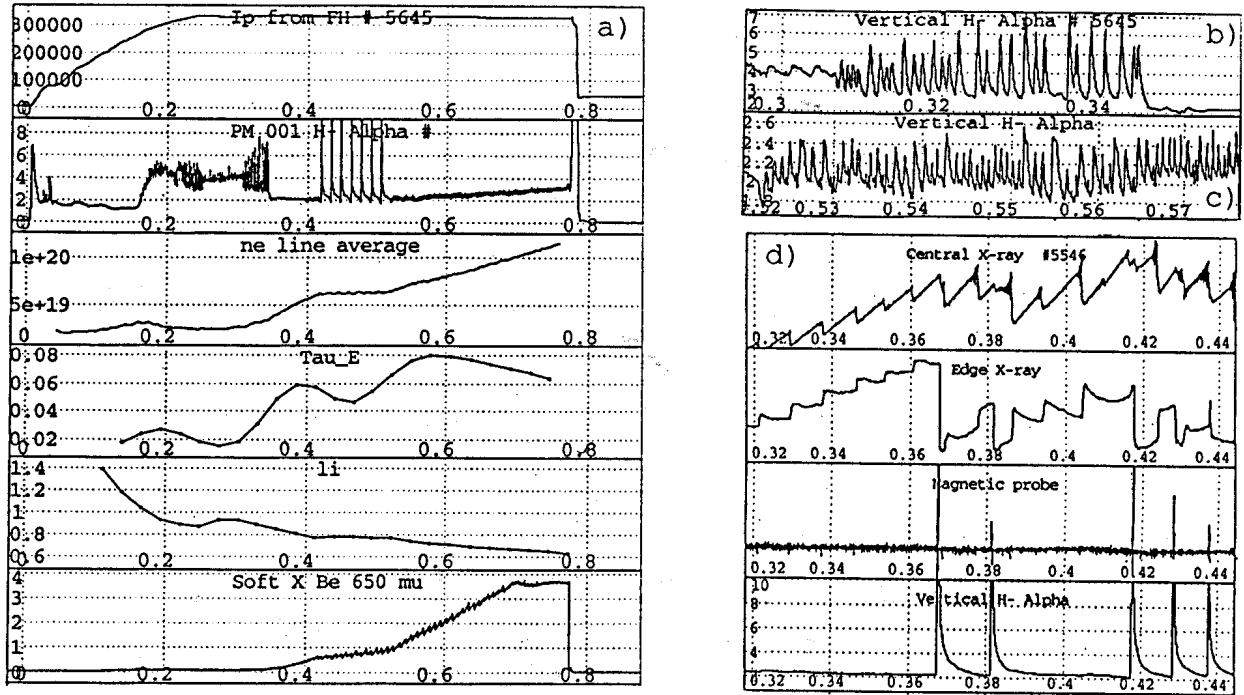


**Fig.3** Diverted H-mode discharge a) time evolution with  $I_p$ ,  $D_{\alpha}$ ,  $\langle n_e \rangle$ ,  $\tau_E$ ,  $l_i$ , and central X-ray emission, showing dithering before L-H transition at 0.32 s, quiescent phase, brief grassy ELM phase at 0.4 s preceding large ELMs and a final grassy ELM phase. (b)  $D_{\alpha}$  emission in dithering phase and c) with grassy ELMs. d) modulation of edge X-ray emission (middle) by sawteeth (top) and large ELMs (bottom).



Power spectrum shot #5547